LETTERS
https://doi.org/10.1038/s41550-021-01469-y

nature astronomy

# The palaeoinclination of the ancient lunar magnetic field from an Apollo 17 basalt

Claire I. O. Nichols[1,2]✉, Benjamin P. Weiss[1], Brenna L. Getzin[1], Harrison H. Schmitt[3], Annemarieke Béguin[4], Auriol S. P. Rae[5,6] and Jay Shah[1]

**Palaeomagnetic studies of Apollo samples indicate that the Moon generated a magnetic field for at least 2 billion years[1,2]. However, the geometry of the lunar magnetic field is still largely unknown because the original orientations of essentially all Apollo samples have not been well constrained. Determining the direction of the lunar magnetic field over time could elucidate the mechanism by which the lunar dynamo was powered and whether the Moon experienced true polar wander. Here we present measurements of the lunar magnetic field 3.7 billion years ago as recorded by Apollo 17 mare basalts 75035 and 75055. We find that 75035 and 75055 record a mean palaeointensity of ~50 μT. Furthermore, we could infer from the magnetization direction of 75055 and the layering of its parent boulder that the inclination of the magnetic field at the time was 34 ± 10°. Our recovered inclination is consistent with, but does not require, a selenocentric axial dipole (SAD) field geometry: a dipole in the centre of the Moon and aligned along the spin axis. Additionally, although true polar wander is not required by our data, true polar wander paths inferred from some independent studies of lunar hydrogen deposits and crustal magnetic anomalies[4–6] are consistent with our measured paleoinclination.**

Unambiguous constraints on lunar palaeomagnetism have almost exclusively been limited to palaeointensity data due to an absence of samples collected during the Apollo missions with known original orientations at the time of magnetization acquisition. Only two palaeomagnetic studies of Apollo samples have attempted to constrain the palaeodirection of the lunar magnetic field[3,4]. Both studies attempted to infer the field's palaeoinclination using magnetic anisotropy measurements, but our analyses of mare basalts find magnetic anisotropy to be a poor indicator of palaeohorizontality (Supplementary Tables 7 and 8 and Supplementary Figs. 12 and 13). We also found that microscopic petrographic fabrics are a poor indicator of horizontality (Supplementary Fig. 14). Here, we present a palaeomagnetic study using astronaut photographs of outcrop-scale petrographic fabrics taken from numerous angles to recover structural data from the lunar surface. This photogrammetric approach is used to reconstruct the orientation of sample 75055 on the lunar surface.

Our approach allows the inclination of the ancient lunar magnetic field to be constrained with minimal ambiguity. Numerous previous studies have attempted to constrain the geometry of the ancient magnetic field using spacecraft measurements of the crustal magnetic field. Although some such studies found support for the presence of a selenocentric axial dipole (SAD) geometry from the clustering of some palaeopoles, the palaeopoles as a whole are spread over the entire surface of the Moon[5,6]. The large scatter is likely in part a consequence of the fact that palaeopole inversions depend on numerous assumptions about the nature of the magnetization source (Supplementary Text 3). Therefore, measurement of the palaeomagnetic directions recorded by lunar samples, whose original orientations can be reconstructed and that can be demagnetized to remove confounding magnetic overprints and dated with radiometric techniques, is likely the most robust approach to reconstruct reliable lunar palaeopoles.

Although there is strong evidence for the existence of a past lunar dynamo, its physical mechanism and power source are highly uncertain. The small size of the lunar core means that the apparent surface palaeointensities before 3.5 Gyr ago (Ga hereafter) imply a very strong dynamo field (>24 mT) in the core even in the limiting case of a purely dipolar field. As a result, convective core dynamo scaling laws fail by more than an order of magnitude to generate surface intensities >50 μT over time periods lasting >30 Myr (ref. [7]). Precession-driven dynamos, although potentially able to achieve higher palaeointensities[8], struggle to generate magnetic fields in spherical cores for realistic viscosities[9] although the dissipative heat from precession might instead serve as a heat source for a convective dynamo[10]. Impact-driven dynamos that initiate mantle stirring of the core may be able to generate the observed palaeointensities, but can be sustained for only thousands of years[11] and require basin-forming impacts that ceased before 3.7 Ga (ref. [12]). It has also been proposed that a basal magma ocean could generate the observed intensity and longevity of the lunar dynamo, but this requires the magma ocean to have an exceptionally high electrical conductivity[13]. Measurements of the geometry of the ancient lunar magnetic field would provide invaluable constraints for distinguishing between these potential dynamo mechanisms, as well as between dynamo and non-dynamo processes (Fig. 1, Supplementary Fig. 19 and Supplementary Text 5).

The relationship between magnetic inclination, $I$, and latitude, $\lambda$, of an axial dipolar magnetic field is given by

$$\tan I = 2 \tan \lambda. \quad (1)$$

The relative contributions of an axial dipole and multipolar terms to a dynamo field can be estimated from the local Rossby number, $Ro_l$,

[1]Department of Earth, Atmospheric and Planetary Sciences, Massachusetts Institute of Technology, Cambridge, MA, USA. [2]Department of Earth Sciences, University of Oxford, Oxford, UK. [3]Department of Engineering Physics, University of Wisconsin-Madison, Madison, WI, USA. [4]Paleomagnetic Laboratory Fort Hoofddijk, Department of Earth Sciences, Utrecht University, Utrecht, The Netherlands. [5]Institute of Earth and Environmental Sciences – Geology, Albert-Ludwigs-Universität Freiburg, Freiburg, Germany. [6]Department of Earth Sciences, University of Cambridge, Cambridge, UK.
✉e-mail: claire.nichols@earth.ox.ac.uk

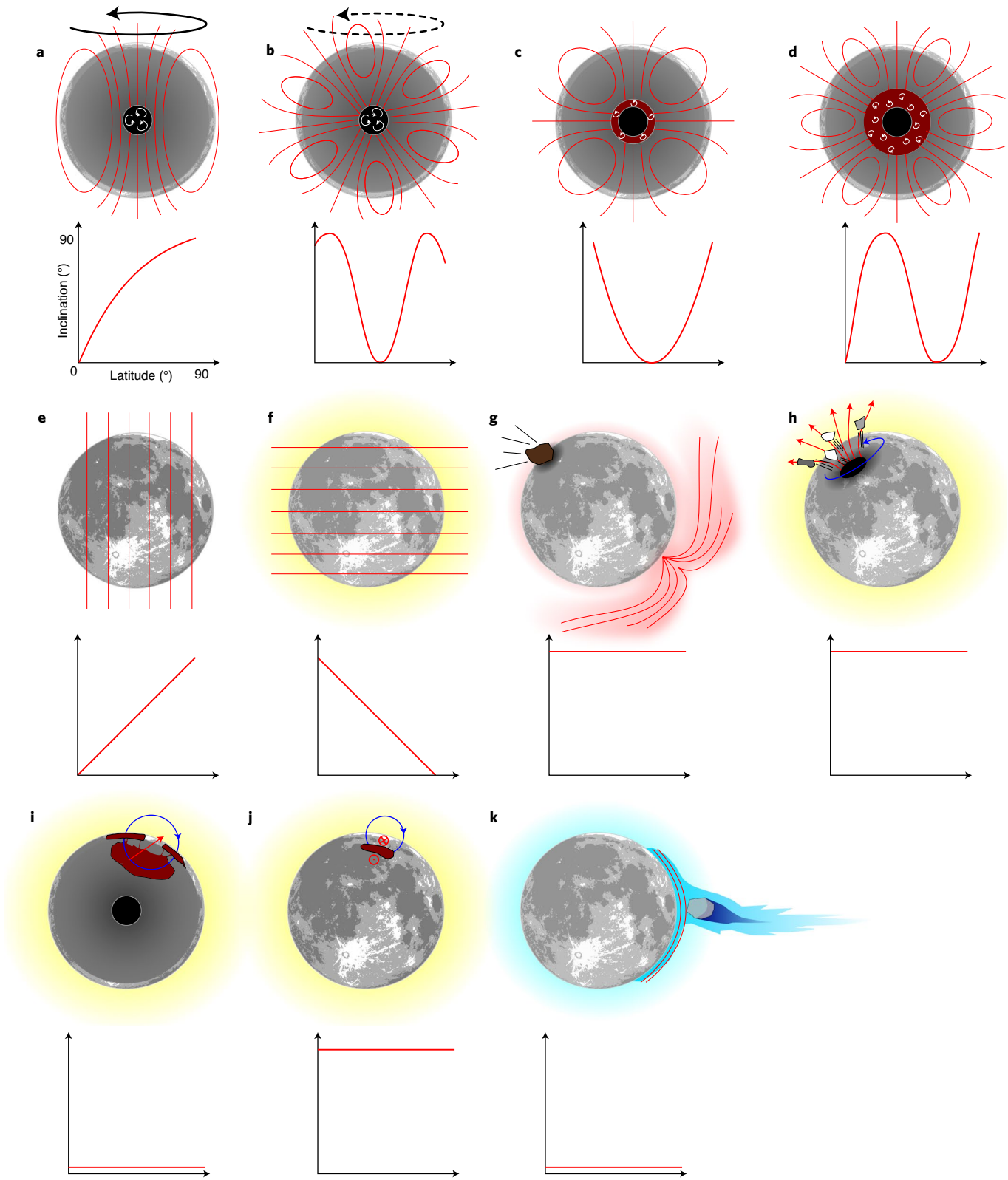


which quantifies the ratio of inertial to Coriolis forces for characteristic flow scales within the core[14]. Synchronous rotation of the Moon was likely established early in lunar history, such that by 3.7 Ga the rotation rate was sufficiently slow ($\sim 5\times10^{-6}\,\mathrm{rad\,s^{-1}}$) that its $\mathrm{Ro_l}$ would have reached a value of ~2, suggesting that the field in the core was dominantly nondipolar[14]. Therefore, we should not expect the lunar dynamo to have followed equation (1). Even so, a high $\mathrm{Ro_l}$ does not by itself preclude a dipolar surface magnetic field geometry. The multipolar state implied by the high $\mathrm{Ro_l}$ applies to only the field-generating region in the core, whereas palaeomagnetic observations constrain only the surface field (Supplementary Text 4).

To constrain the geometry and intensity of the ancient lunar dynamo, we studied two mare basalts collected during the Apollo 17 mission: 75035 and 75055. These samples have indistinguishable

**Fig. 1 | Hypothesized magnetic field sources for lunar palaeomagnetism.** The top and bottom of each panel show a schematic of the approximate field direction with respect to the Moon and the inclination as a function of latitude, respectively. In the top panels, black represents the core, grey represents solid silicates, dark red represents molten silicate, red lines represent the magnetic field, blue lines represent electrical currents and the yellow exterior region represents the solar wind for cases in which it is invoked for field generation. **a**, A selenocentric axial dipolar magnetic field generated by a core dynamo with a rapid planetary rotation rate ($Ro_l < 0.12$). **b**, A multipolar, non-axisymmetric magnetic field generated by a core dynamo with a slow planetary rotation rate ($Ro_l > 0.12$). **c**, An axially aligned quadrupolar dynamo generated by a deep magma ocean dynamo[13]. **d**, An axially aligned octupolar dynamo generated by a shallow magma ocean dynamo[13]. **e**, The Earth's mean axial dipole field at the location of the Moon. **f**, The interplanetary magnetic field. **g**, Antipodal field amplified by basin-forming impacts[52]. The predicted inclination is for rocks at the crater antipode. **h**, Fields generated by impact plasmas[53]. The predicted inclination is for rocks directly below the crater. **i**, Magnetic fields generated by the thermoelectric effect in lava basins that are electrically connected to subsurface magma and the solar wind[53,54]. **j**, Magnetic fields generated by a unipolar dynamo in lava basins[53]. The predicted inclination is for a rock at the surface close to the lava pool. **k**, Compression of the interplanetary magnetic field around the Moon by a cometary coma[53].

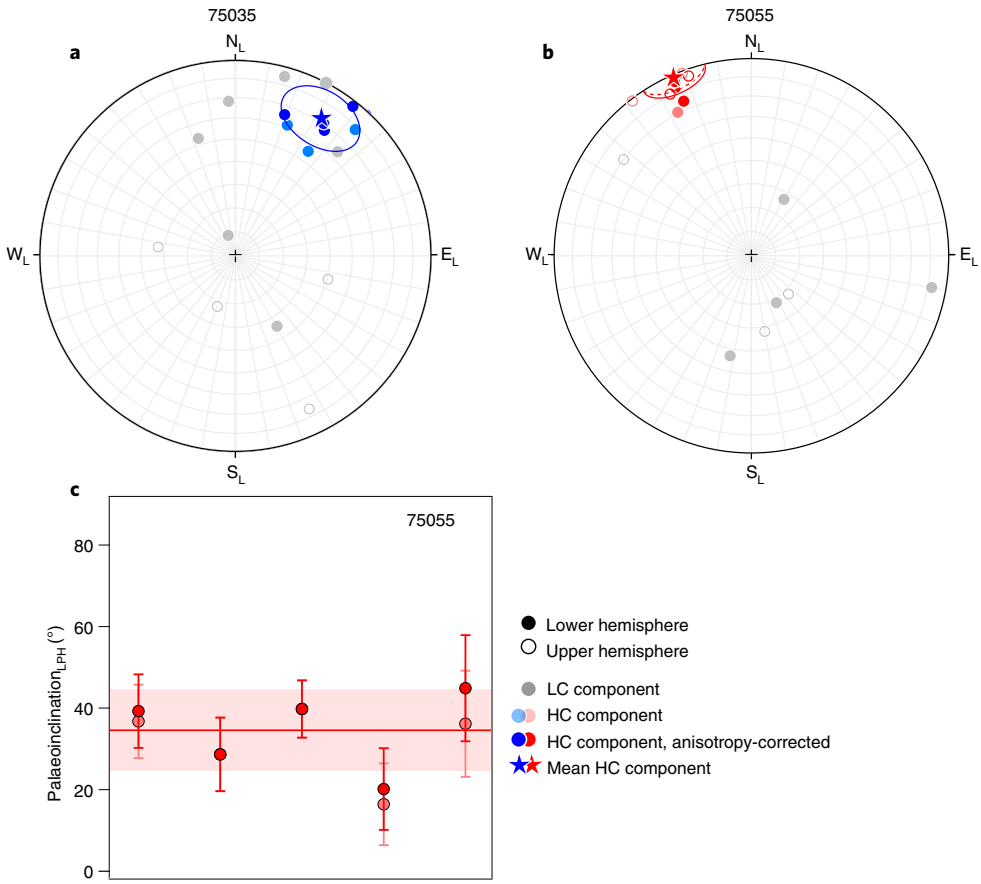


**Fig. 2 | NRM components in 75035 and 75055 and associated palaeoinclinations.** The low-coercivity (LC, grey) and origin-trending high-coercivity (HC, pale blue for 75035 and pale red for 75055) components are shown in present-day lunar (L) coordinates for individual specimens. Remanence-anisotropy-corrected high-coercivity components are shown in deep blue and red for 75035 and 75055, respectively. Samples of 75035 with bandsaw overprints are omitted. The mean (stars) and 95% confidence interval (ellipses) were calculated for the anisotropy-corrected high-coercivity components. **a**,**b**, Equal-area stereonet projections of mutually oriented specimen components for 75035 (**a**) and for 75055 (**b**) in lunar coordinates. **c**, Palaeoinclinations in lunar palaeohorizontal coordinates for the high-coercivity, origin-trending components in 75055. The mean (horizontal red line) and one standard deviation (red shaded region) are shown for anisotropy-corrected components. Uncertainties correspond to the measured maximum angular deviation (Supplementary Table 11).

Pb–Pb ages of 3,753 ± 9 Ma and 3,752 ± 9 Ma, respectively[15]. They were collected at the rim of the 610-m-diameter, ~500 ± 200 Myr-old Camelot crater[16] located at 20.2° N, 37.3° E. The Camelot cratering event is thought to have exposed >120 m of mare basalt flow stratigraphy. The possibility that the original orientations of these samples could be reconstructed only recently came to light following reassessment of the geology of the Taurus–Littrow valley[16]. Although they were originally interpreted as ejecta blocks, the parent boulders of these samples are now thought to represent near-in-situ wall rock as evidenced by the absence of an ejecta blanket. New interpretations suggest Camelot crater is 400 Myr older than previously thought and has undergone extensive mass wasting to expose wall rock while the ejecta blanket was ground into regolith. It is unlikely that these boulders have moved more than ~10 m from their original location, although they may have been differentially tilted or rotated with respect to the underlying bedrock[16].

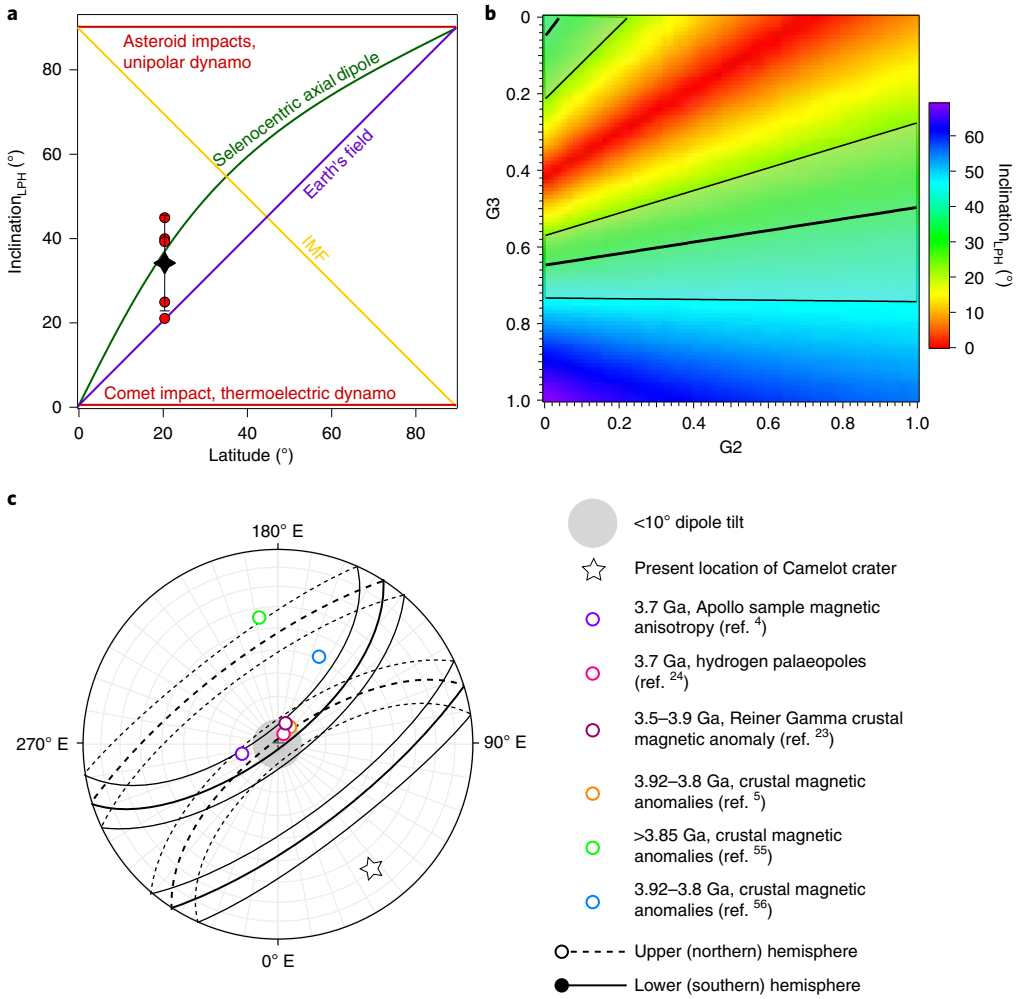


**Fig. 3 | Predictions for the palaeoinclination of the lunar field and implications for multipolarity and true polar wander. a**, Palaeoinclination results are shown at the present latitude of Camelot crater by the black symbol with 95% uncertainty calculated from paleomagnetic analyses. Red dots are the measured palaeoinclinations from each specimen of 75055. Predicted inclination versus latitude curves (see Fig. 1) are shown for impact fields, a unipolar dynamo and a thermoelectric dynamo (red lines), Earth's magnetic field (purple line), the interplanetary magnetic field (IMF, yellow line) and a selenocentric axial dipole (green line). **b**, The predicted magnetic inclination at Camelot crater for a magnetic field with zonal dipolar, quadrupolar and octupolar components, where G2 and G3 are the quadrupolar-to-dipolar and octupolar-to-dipolar field ratios, respectively. The thick black line is the mean palaeoinclination and the regions bounded by thin black lines represent the 95% confidence interval. Both low and high degrees of multipolarity are permitted by our measured palaeoinclination. **c**, Equal-area stereographic projection showing the possible palaeopole locations 3.7 Ga in present-day lunar geographic coordinates. Open symbols and dashed lines are in the northern hemisphere, and closed symbols and solid lines are in the southern hemisphere. The star is the current location of Camelot crater where the samples were collected. The thick black lines are the permitted locations of the north pole calculated from our mean recovered palaeoinclination. Thin black lines mark the 95% confidence interval for our measurement. Two bands are permitted given the possibility of a reversing dynamo. The grey shaded region represents <10° dipole tilt. North palaeopole locations 3.7 Ga from independent studies are shown in purple[4], pink[24], red[23], orange[5], green[55] and blue[56].

The parent boulder for 75055 exhibits clear layering and planar features that can be used to infer palaeohorizontality. Sample 75055 is therefore one of very few known Apollo samples whose original orientation can be unambiguously constrained. We have used this sample to measure the palaeoinclination (along with the palaeointensity) of the lunar field 3.7 Ga. Because the parent boulder of 75035 is smaller and was documented with fewer astronaut photographs, we can only infer the field paleointensity from this sample.

Electron microscopy and rock magnetic analyses indicate that the magnetic carriers in our samples are pure Fe kamacite (Supplementary Figs. 7 and 8, Supplementary Table 3 and Supplementary Text 2). Our alternating-field demagnetization of specimens of 75035 and 75055 revealed non-origin-trending low-coercivity components of natural remanent magnetization (NRM) that were removed by 0–11 mT (Extended Data Fig. 1 and Supplementary Table 11). The low-coercivity components are highly scattered within each parent sample (Fig. 2). Once the low-coercivity overprints were removed, we found that four non-bandsawn specimens of 75035 and five specimens of 75055 each contained a final origin-trending high-coercivity component that was blocked up to 40–60 mT (similar directions can be recovered up to 145 mT, but with less certainty) and is essentially unidirectional within each parent sample (Extended Data Fig. 1 and Supplementary Table 11). The Fisher mean anisotropy-corrected high-coercivity direction for these four specimens of 75035 is 032°/18° in present-day lunar coordinates (see Table 1 for definitions and descriptions of coordinate systems) with a 95% confidence interval of $\alpha_{95} = 14°$. The Fisher mean anisotropy-corrected high-coercivity direction

**Table 1 | Definitions and descriptions of the coordinate systems used throughout this study**

| Coordinate system | Abbreviation | Description | Samples |
|---|---|---|---|
| Magnetometer | mag | The coordinate system of the superconducting rock magnetometer for AARM measurements at the Fort Hoofddijk Paleomagnetic Laboratory. | |
| Laboratory | lab | Orientation used at the Massachusetts Institute of Technology Paleomagnetism Laboratory. | 75035 |
| JSC | JSC | Orientation used at the Johnson Space Center to document Apollo samples. | 75035, 75055 |
| Present-day lunar | L | Orientation on the lunar surface, where 'Top' is outward normal from the lunar surface and 'North' is horizontal and toward the present-day spin axis. | 75035, 75055 |
| Lunar palaeohorizontal | LPH | Using planar features on blocks, lunar coordinates are tilt-corrected to the palaeohorizontal. Only inclination is considered in this coordinate system. | 75055 |

The order in which coordinate systems are listed is the order in which corrections were made to sample orientations throughout the study.

for the five specimens of 75055 in present-day lunar coordinates is 334°/00° with $\alpha_{95}=10°$. In lunar palaeohorizontal (LPH) coordinates, the high-coercivity component of 75055 has a palaeoinclination of $I_{LPH}=34°$ with $\alpha_{95}=10°$, and an estimated Fisher precision parameter of $\kappa=61.6$ where the uncertainty is estimated from the scatter in the high-coercivity directions among individual specimens (Supplementary Table 9).

We measured mean high-coercivity palaeointensities of $50.7\pm13.5\,\mu T$ and $57.0\pm17.3\,\mu T$ ($1\sigma$ standard error for four and eight specimens) for 75035 and 75055, respectively, using the anhysteretic remanent magnetization (ARM) method (Supplementary Figs. 15 and 16 and Supplementary Table 10). The palaeointensity estimates for 75035 and 75055 are both within error of the mean value of 77 μT measured from six previously measured Apollo samples of age 3.5–4.2 Gyr (refs. [4,12,17,18]). These results thereby provide additional evidence that >3.5 Ga, the Moon had an active dynamo generating a strong magnetic field.

We consider the implications of our palaeoinclination results based on two alternative assumptions about the palaeoinclination record for 75055; first, that it reflects only the instantaneous lunar magnetic field and, second, that it is representative of the time-averaged (over ~0.1–10 Myr) lunar field. Considering the instantaneous magnetic field, we calculated the possible locations of the virtual magnetic pole. As the palaeoazimuth is unconstrained, the possible virtual magnetic pole locations define two small circles (Fig. 3c). For our recovered palaeoinclination, the dipole tilt is permitted (but not required) to be <10°, the maximum degree of tilt expected for an axially aligned instantaneous magnetic field that is dipole-dominated like those of other inner solar system bodies[19].

We next consider our palaeoinclination results assuming that the instantaneous and time-averaged lunar magnetic fields were similar (that is, that the recorded inclination reflects a durable feature of the lunar field geometry). We consider both a multipolar core dynamo field and implications for true polar wander. To assess different magnetic field sources, we assume that Camelot crater was at its present latitude at the time of NRM acquisition. Using equation (1) and assuming no subsequent true polar wander, the magnetic inclination of a SAD at Camelot crater would be ~36°, which is indistinguishable from our palaeoinclination estimates (Fig. 3a). Because a dipolar magnetic field is at odds with the high $Ro_l$ of the Moon, this could indicate that the lunar core is stratified[20–22] and/or that the dynamo mechanism was non-convective (for example, precession[8,10]).

Although our recovered palaeoinclination is consistent with a SAD generated by a core dynamo, our results do not require such a geometry. For example, our data cannot exclude a substantial multipolar contribution from low-order, purely zonal terms (Fig. 3b). A multipolar magnetic field is consistent with the low lunar rotation rate, and would also be favoured by dynamo sources closer to the surface (for example, a basal magma ocean[13]) given the $r^{-(l+2)}$ dependence of multipolar fields, where $r$ is the distance from the top of the core, and $l$ is the spherical harmonic degree. The observed clustering of palaeopoles near the poles and the equator would also be consistent with a predominantly quadrupolar dynamo or a persistent non-axial dipole field[23].

Finally, we consider the implications of our palaeoinclination for true polar wander, assuming that our measured palaeoinclination corresponds to a SAD. Considering the possibility that a SAD may have reversed, our palaeoinclination measurement predicts palaeopole locations offset from the spin axis that are indistinguishable from those of several independent studies at ~3.7 Ga (refs. [4,5,23,24]), although true polar wander is not required to explain our results (Fig. 3c and Supplementary Figs. 17 and 18).

We were able to reconstruct the palaeohorizontal orientation of the parent block for 75055 from planar features documented in astronaut photographs. This has enabled an accurate measurement of palaeoinclination at a known latitude on the lunar surface. The recovered palaeoinclination is consistent with, but does not require, a SAD. In addition, our palaeointensity measurements have shown that both 75035 and 75055 cooled in the presence of a strong field (~50 μT), consistent with previous evidence for an epoch of intense magnetic fields ~3.5–4.2 Ga (ref. [1]).

Most importantly, we have provided a framework in which other potentially orientable Apollo samples can be included to improve our understanding of the ancient lunar magnetic field. Contemporaneous measurements of the ancient lunar field from samples at different latitudes on the Moon will enable the magnetic field geometry to be unambiguously determined. Palaeoinclination measurements from samples of different ages would also enable the rate and extent of true polar wander and lunar secular variation to be quantified. Future sample return missions to the Moon should collect oriented samples from confirmed bedrock, which will greatly enhance our understanding of the geometry and temporal variability of the ancient lunar magnetic field and the mechanism of dynamo generation.

## Methods

**Reconstructing sample orientation relative to the lunar surface.** In this study, we analysed subsamples 75035,242 and 75055,127, which B.P.W. and H.H.S. selected and oriented at the Johnson Space Center (JSC) in 2016. Our subsamples are oriented with respect to their parent samples in JSC coordinates (see Table 1 for details of coordinate systems). We reconstructed the orientations of parent samples of 75035 and 75055 relative to their sampling positions on the lunar surface using JSC and astronaut photographs and transcripts recorded by astronauts H.H. Schmitt and E.A. Cernan during sample collection. Both 75035 and 75055 were hammered directly off blocks with visible planar features at the edge of Camelot crater by astronaut H.H. Schmitt in December 1972 (Extended Data Fig. 2). The blocks were photographed before and after sampling by astronauts H.H. Schmitt and E.A. Cernan. The present-day orientations of 75035 and 75055 relative to

each block on the lunar surface were reconstructed using photographs taken under lunar-lighting conditions simulated at the Lunar Receiving Laboratory[25]. The astronaut photographs indicate that the blocks were likely not undisturbed bedrock when samples 75035 and 75055 were collected but rather had undergone subsequent tilting and rotation since their formation (Extended Data Fig. 3). As a result, outcrop textural features allow the palaeohorizontal to be determined, but cannot account for the palaeoazimuthal direction. We therefore only attempt to constrain palaeohorizontal and determine the ancient field's palaeoinclination and not palaeodeclination.

Planar features are observed on the parent boulders of 75035 and 75055 and on other blocks around Camelot crater (Extended Data Fig. 3). The astronauts noted that these planar features were largely defined by variations in vesicle distribution[26] and may represent the tops of lunar lava flows. Terrestrial analogues thought to be emplaced in a similar manner to mare basalt lava flows are the extensively studied pāhoehoe basalt flows of Hawaii[27–29]. Pāhoehoe flows grow via inflation due to injection of fresh magma beneath a solid crust. This results in a distinct distribution of vesicles, with the bottom and top of the lava flow containing horizontally aligned 'vesicular zones' that can be tens of centimetres to metres in thickness, whereas horizontal 'vesicle sheets' (~10 cm thickness) form near the centre of the flow. 75035 and 75055 are thought to have formed in the central part of a pāhoehoe-like flow given the coarse (>1 mm) crystalline nature of ilmenite within the samples[29,30], such that the planar features observed on the parent boulder of 75055 likely correspond to vesicle sheets. The spatial distribution of features is consistent with a lava flow thickness of <10 m. Lunar lava flows have a lower viscosity than that of any known terrestrial flow[31] and are thin (<10 m) and laterally extensive[32]. It should also be noted that horizontal vesicular layers can be produced without the injection of fresh melt into the system[33]. In terrestrial basalts exhibiting vesicular layers, such as the Columbia River flood basalt flows, vesicles have been observed to form approximately every 1 m, consistent with theoretical calculations[33]. However, given the lower viscosity of lunar basalts and lunar gravity, these layers are likely to be closer together on the Moon due to faster rise times and are therefore a plausible explanation for the ~30 cm spacing between vesicle layers observed on the blocks at Camelot crater (Extended Data Fig. 3). We therefore assumed that the planar features defined by vesicles within the 75055 parent block represent the palaeohorizontal at the time of eruption. Using this assumption, we reconstructed the palaeohorizontal orientation of the block. Note also that the similar compositions of the blocks at the crater edge and their spatial distribution indicate that they are close to their formation localities such that the measured palaeointensities and palaeoinclinations can be interpreted in the context of the latitude of Camelot crater.

We used photographs of sample 75055 (in JSC coordinates) to reconstruct its original orientation in lunar geographic coordinates (Supplementary Figs. 4 and 6). For 75035, the small number of astronaut photographs and their limited range of perspectives means that we cannot unambiguously reconstruct the palaeohorizontal for this sample (Supplementary Figs. 3 and 5). The attitude of the visible foliations on the parent boulder of 75055 were reconstructed by measuring the apparent trend and plunge of planar features observable in a series of photographs taken from different locations (Supplementary Table 2 and Extended Data Fig. 4). A great circle was fitted to the trend and plunge measurements to define the plane. The planar features have a strike and dip of 243°/36° ($\alpha_{95}=5°$) in lunar coordinates. The orientation of the plane was used to tilt the boulder back to its original palaeohorizontal position. Once the palaeohorizontal orientation of the parent boulder of 75055 was established, the magnetic palaeoinclination was recovered. Because the lunar magnetic field may have undergone reversals, it is only meaningful to recover the magnitude of the palaeoinclination and not its sign.

**Palaeomagnetic analysis.** All demagnetization experiments were conducted on a 2G Enterprises Superconducting Rock Magnetometer 755 at the Massachusetts Institute of Technology Paleomagnetism Laboratory. The magnetometer has a sensitivity of $<1\times10^{-12}$ A m$^2$ (ref. [34]). Fifteen specimens of 75035 and nine specimens of 75055 were demagnetized using an alternating field because thermal demagnetization can cause thermochemical alteration of mare basalts even under controlled-atmosphere conditions (Supplementary Fig. 9)[35,36]. The NRM was removed by three-axis alternating-field demagnetization in steps of 0.5 mT up to 25 mT, steps of 1 mT up to 95 mT, and then steps of 1.5 mT up to 145 mT. The magnetic moment was measured after each alternating-field step and the three orthogonal measurements were then averaged to correct for gyroscopic remanent magnetization following the Zijderveld–Dunlop method[35,37]. A subset of specimens (75055,127Aa, 75055,127Ab, 75055,127Ac, 75055,127Ae and 75055,127b) were demagnetized up to 420 mT in steps of 7.5 mT to ensure that high-coercivity components were entirely removed.

NRM components were characterized using principal component analysis. Origin-trending components were identified when the maximum angular deviation (MAD) exceeded the angular deviation. The final fits for such origin-trending components were anchored to the origin[38,39]. These fits were used to calculate a Fisher mean direction and associated 95% confidence interval ($\alpha_{95}$) for each specimen in PmagPy 3.0[40]. Six specimens of 75035 exhibited resolvable origin-trending high-coercivity components with a MAD < 30°, but two of these were disregarded (75035Ad and 75035Ah) because they were partially overprinted by bandsawing at JSC (Supplementary Figs. 1 and 2 and Supplementary Table 1). Five specimens of 75055 exhibited resolvable origin-trending high-coercivity components with a MAD < 30°. Component directions were plotted in Stereonet[41,42], rotated to present-day lunar coordinates and, for 75055, tilt-corrected using the reported palaeohorizontal estimates (see 'Reconstructing sample orientation relative to the lunar surface'). Recovered component directions were also corrected for anisotropy of ARM (AARM) (see 'Rock magnetic analysis').

Palaeointensity estimates were calculated using the ARM palaeointensity method[37,43,44]. NRM demagnetization curves were compared to alternating-field demagnetization of an ARM with a 100 μT d.c. bias field applied with a 260 mT alternating field. The thermoremanent magnetization (TRM)-equivalent palaeointensity recorded by the samples is given by

$$P_{\mathrm{ARM}} = \frac{\Delta\mathrm{NRM}}{\Delta\mathrm{ARM}}\frac{b}{f'} \tag{2}$$

where $b$ is the d.c. bias field and $f' = 1.34$ is the TRM/ARM calibration factor experimentally determined using lunar basalts[45]. There are two main uncertainties associated with these palaeointensity estimates. First, the least-squares slope obtained from $\frac{\Delta\mathrm{NRM}}{\Delta\mathrm{ARM}}$ has an uncertainty associated with scatter in the data around the best-fit line. Second, the calibration factor $f'$ is estimated to have a $2\sigma$ uncertainty of a factor of 5 (ref. [1]). The uncertainty in $f'$ originates from its dependence on ferromagnetic mineralogy including grain size, grain morphology and grain distribution. Cooling-rate corrections are not applied because the heating time (~1 h) for ARM/TRM calibration experiments is similar to the several-day cooling timescales of 75035 and 75055 (refs. [46,47]).

**Rock magnetic analysis.** We used several rock magnetic techniques to assess the fidelity and magnetic recording properties of samples 75035 and 75055 (Supplementary Text 1). We conducted palaeointensity fidelity tests, isothermal remanent magnetization (IRM) acquisition and Curie balance analysis, and quantified the degree of AARM.

To assess the magnetic recording fidelity of samples 75035 and 75055, we gave the samples ARMs in d.c. bias fields ranging from 5 μT to 100 μT and quantified how accurately we could recover the palaeointensity of this field using the ARM palaeointensity method. The ARMs were applied with an alternating field of 260 mT and were alternating-field demagnetized following the same protocol that was used to demagnetize the NRM. The demagnetization curves were compared to the demagnetization curve of the 100 μT ARM. For each applied ARM, the difference, $D' = \frac{L-I}{L}$, between the recovered palaeointensity ($I$) and the predicted equivalent TRM ($L$) and the error, $E = \frac{W}{L}$, based on the 95% confidence for the retrieved palaeointensity ($W$) were calculated[35,48]. Acceptance criteria for a reliable palaeomagnetic recorder are defined by $-50\% < D' < 100\%$ and $E < 50\%$ (Supplementary Table 4 and Supplementary Fig. 11).

We conducted IRM acquisition to assess the coercivity spectrum of magnetic carriers in each sample. Specimens were given a saturation IRM of 400 mT and were then alternating-field demagnetized. The derivative of the demagnetization curve with respect to the applied field, δIRM/δ$B$, was calculated to infer the coercivity distribution (Supplementary Fig. 10).

The samples' magnetic mineralogy and susceptibility to thermochemical alteration were assessed using a Curie balance at the Fort Hoofddijk Paleomagnetic Laboratory. A small (3.52 mg) fragment of specimen 75055Ac was exposed to fields of 100–300 mT during a heating cycle from room temperature to 800 °C and then back to room temperature in air. The magnetization was measured every second over the course of the experiment, which took ~12 h. Raw data were smoothed using a Savitzky–Golay filter[49].

The AARM of seven specimens of 75035 and six specimens of 75055 was measured at the Fort Hoofddijk Paleomagnetic Laboratory using a 2G Enterprises Superconducting Rock Magnetometer. Specimens were given an ARM of 50 μT in an alternating field of 150 mT. Samples were given an ARM in nine distinct orientations, $E_{mag}$, $N_{mag}$, $T_{mag}$, $NE_{mag}$, $NW_{mag}$, $TE_{mag}$, $TW_{mag}$, $TN_{mag}$ and $TS_{mag}$, with each specimen mounted in a different orientation in laboratory coordinates to remove any directional measurement bias (Supplementary Table 5). After measuring the magnitude and orientation of the acquired ARM, specimens were alternating-field demagnetized up to 150 mT in three orthogonal directions. The order of the ARM and demagnetization steps is shown in Supplementary Table 6. Specimens were mounted in custom-made glass cubes with three-dimensional-printed sample holders (holder moment $<7\times10^{-11}$ A m$^2$) to maintain exact orientations throughout. This enabled the estimation of the three principal axes defining the anisotropy ellipsoid, where $p_1$ is the maximum, $p_2$ is the intermediate and $p_3$ is the minimum principal axis of anisotropy[50]. After defining the axes, we calculated the degree of foliation $F = \frac{p_2}{p_3}$, lineation $L = \frac{p_1}{p_2}$ and anisotropy $P = \frac{p_1}{p_3}$ for individual specimens[51]. Anisotropy corrections improved the clustering of directions for 75035, with the Fisher precision parameter, $\kappa$, increasing from 11.9 to 19.1, whereas for 75055 $\kappa$ decreased slightly from 49.2 to 42.9 (Fig. 2).

## Data availability

The palaeomagnetic data that support the findings of this study are available from the Magnetic Information Consortium (MagIC) database at http://www2.earthref.

org/MagIC/17123. All other data requests and correspondence should be directed to C.I.O.N. Source data are provided with this paper.

Received: 9 March 2021; Accepted: 27 July 2021;
Published online: 27 September 2021

## References

1. Weiss, B. P. & Tikoo, S. M. The lunar dynamo. *Science* **346**, 1246753 (2014).
2. Tikoo, S. M. et al. A two-billion-year history for the lunar dynamo. *Sci. Adv.* **3**, e1700207 (2017).
3. Potter, D. K. Novel magnetic techniques for rapidly detecting palaeomagnetically important single-domain iron particles and obtaining directional palaeomagnetic data from 'unoriented' lunar rock samples. *Can. Aeronaut. Space J.* **57**, 12–23 (2011).
4. Cournède, C., Gattacceca, J. & Rochette, P. Magnetic study of large Apollo samples: possible evidence for an ancient centered dipolar field on the Moon. *Earth Planet. Sci. Lett.* **331-332**, 31–42 (2012).
5. Hood, L. L. Central magnetic anomalies of Nectarian-aged lunar impact basins: probable evidence for an early core dynamo. *Icarus* **211**, 1109–1128 (2011).
6. Oliveira, J. S. & Wieczorek, M. A. Testing the axial dipole hypothesis for the Moon by modeling the direction of crustal magnetization. *J. Geophys. Res. Planets* **122**, 383–399 (2017).
7. Evans, A. J., Tikoo, S. M. & Andrews-Hanna, J. C. The case against an early lunar dynamo powered by core convection. *Geophys. Res. Lett.* **45**, 98–107 (2018).
8. Dwyer, C. A., Stevenson, D. J. & Nimmo, F. A long-lived lunar dynamo driven by continuous mechanical stirring. *Nature* **479**, 212–214 (2011).
9. Cébron, D., Laguerre, R., Noir, J. & Schaeffer, N. Precessing spherical shells: flows, dissipation, dynamo and the lunar core. *Geophys. J. Int.* **219**, S34–S57 (2019).
10. Stys, C. & Dumberry, M. A past lunar dynamo thermally driven by the precession of its inner core. *J. Geophys. Res. Planets* **125**, e2020JE006396 (2020).
11. Le Bars, M., Wieczorek, M. A., Karatekin, Ö., Cébron, D. & Laneuville, M. An impact-driven dynamo for the early Moon. *Nature* **479**, 215–218 (2011).
12. Suavet, C. et al. Persistence and origin of the lunar core dynamo. *Proc. Natl Acad. Sci. USA* **110**, 8453–8458 (2013).
13. Scheinberg, A. L., Soderlund, K. M. & Elkins-Tanton, L. T. A basal magma ocean dynamo to explain the early lunar magnetic field. *Earth Planet. Sci. Lett.* **492**, 144–151 (2018).
14. Olson, P. & Christensen, U. R. Dipole moment scaling for convection-driven planetary dynamos. *Earth Planet. Sci. Lett.* **250**, 561–571 (2006).
15. Snape, J. F. et al. The timing of basaltic volcanism at the Apollo landing sites. *Geochim. Cosmochim. Acta* **266**, 29–53 (2019).
16. Schmitt, H. H. et al. Revisiting the field geology of Taurus–Littrow. *Icarus* **298**, 2–33 (2017).
17. Garrick-Bethell, I., Perera, V., Nimmo, F. & Zuber, M. T. The tidal–rotational shape of the Moon and evidence for polar wander. *Nature* **512**, 181–184 (2014).
18. Shea, E. K. et al. A long-lived lunar core dynamo. *Science* **335**, 453–456 (2012).
19. Schubert, G. & Soderlund, K. M. Planetary magnetic fields: observations and models. *Phys. Earth Planet. Inter.* **187**, 92–108 (2011).
20. Weber, R. C., Lin, P.-Y., Garnero, E. J., Williams, Q. C. & Lognonné, P. Seismic detection of the lunar core. *Science* **331**, 309–312 (2011).
21. Christensen, U. R. A deep dynamo generating Mercury's magnetic field. *Nature* **444**, 1056–1058 (2006).
22. Takahashi, F., Shimizu, H. & Tsunakawa, H. Mercury's anomalous magnetic field caused by a symmetry-breaking self-regulating dynamo. *Nat. Commun.* **10**, 208 (2019).
23. Maxwell, R. E. & Garrick-Bethell, I. Evidence for an ancient near-equatorial lunar dipole from higher precision inversions of crustal magnetization. *J. Geophys. Res. Planets* **125**, e06567 (2020).
24. Siegler, M. A. et al. Lunar true polar wander inferred from polar hydrogen. *Nature* **531**, 480–484 (2016).
25. Wolfe, E. W. et al. *The Geologic Investigation of the Taurus-Littrow Valley; Apollo 17 Landing Site, with a Section on Apollo 17 Lunar Surface Photography* Professional Paper 1080 (Astrogeology Science Center, U.S. Government Publishing Office, 1981).
26. Meyer, C. *Lunar Sample Compendium* (Astromaterials Research & Exploration Science, 2010); http://curator.jsc.nasa.gov/lunar/lsc/
27. Cashman, K. V., Thornber, C. R. & Kauahikaua, J. P. Cooling and crystallization of lava in open channels, and the transition of pāhoehoe lava to 'a'ā. *Bull. Volcanol.* **61**, 306–323 (1999).
28. Self, S., Keszthelyi, L. & Thordarson, T. The importance of pāhoehoe. *Annu. Rev. Earth Planet. Sci.* **26**, 81–110 (1998).
29. Donohue, P. H. & Neal, C. R. Quantitative textural analysis of ilmenite in Apollo 17 high-titanium mare basalts. *Geochim. Cosmochim. Acta* **149**, 115–130 (2015).
30. Brown, G. M., Peckett, A., Emeleus, C. H., Phillips, R. & Pinsent, R. H. Petrology and mineralogy of Apollo 17 mare basalts. In *Proc. 6th Lunar Science Conference* (ed. Merrill, R. B.) 1–13 (Pergamon Press, 1975).
31. Murase, T. & McBirney, A. R. Viscosity of lunar lavas. *Science* **167**, 1491–1493 (1970).
32. Head, J. W.III Lunar volcanism in space and time. *Rev. Geophys.* **14**, 265–300 (1976).
33. Manga, M. Waves of bubbles in basaltic magmas and lavas. *J. Geophys. Res. Solid Earth* **101**, 17457–17465 (1996).
34. Wang, H. et al. Lifetime of the solar nebula constrained by meteorite paleomagnetism. *Science* **627**, 623–627 (2017).
35. Tikoo, S. M. et al. Magnetic fidelity of lunar samples and implications for an ancient core dynamo. *Earth Planet. Sci. Lett.* **337-338**, 93–103 (2012).
36. Suavet, C., Weiss, B. P. & Grove, T. L. Controlled-atmosphere thermal demagnetization and paleointensity analyses of extraterrestrial rocks. *Geochem. Geophys. Geosyst.* **15**, 2733–2743 (2014).
37. Garrick-Bethell, I., Weiss, B. P., Shuster, D. L. & Buz, J. Early lunar magnetism. *Science* **323**, 356–359 (2009).
38. Kirschvink, J. L. The least-squares line and plane and the analysis of palaeomagnetic data. *Geophys. J. Int.* **62**, 699–718 (1980).
39. Tauxe, L. & Staudigel, H. Strength of the geomagnetic field in the Cretaceous Normal Superchron: new data from submarine basaltic glass of the Troodos Ophiolite. *Geochem. Geophys. Geosyst.* **5**, 2003GC000635 (2004).
40. Tauxe, L. et al. PmagPy: software package for paleomagnetic data analysis and a bridge to the Magnetics Information Consortium (MagIC) Database. *Geochem. Geophys. Geosyst.* **17**, 2450–2463 (2016).
41. Allmendinger, R. W., Cardozo, N. C. & Fisher, D. *Structural Geology Algorithms: Vectors and Tensors* 44–98 (Cambridge Univ. Press, 2013).
42. Cardozo, N. C. & Allmendinger, R. W. Spherical projections with OSXStereonet. *Comput. Geosci.* **51**, 193–205 (2013).
43. Tikoo, S. M. et al. Decline of the lunar core dynamo. *Earth Planet. Sci. Lett.* **404**, 89–97 (2014).
44. Paterson, G. A., Heslop, D. & Pan, Y. The pseudo-Thellier palaeointensity method: new calibration and uncertainty estimates. *Geophys. J. Int.* **207**, 1596–1608 (2016).
45. Stephenson, A. & Collinson, D. W. Lunar magnetic field palaeointensities determined by an anhysteretic remanent magnetization method. *Earth Planet. Sci. Lett.* **23**, 220–228 (1974).
46. Tauxe, L. *Essentials of Paleomagnetism* (Univ. of California Press, 2010).
47. Halgedahl, S. L., Day, R. & Fuller, M. The effect of cooling rate on the intensity of weak-field TRM in single-domain magnetite. *J. Geophys. Res. Solid Earth* **85**, 3690–3698 (1980).
48. Bryson, J. F. J., Weiss, B. P., Harrison, R. J., Herrero-Albillos, J. & Kronast, F. Paleomagnetic evidence for dynamo activity driven by inward crystallisation of a metallic asteroid. *Earth Planet. Sci. Lett.* **472**, 152–163 (2017).
49. Press, W., Teukolsky, S., Vertterling, W. & Flannery, B. in *Numerical Recipes in C: The Art of Scientific Computing* 2nd edn, 650–655 (Cambridge Univ. Press, 1992).
50. Jelinek, V. Characterization of the magnetic fabric of rocks. *Tectonophysics* **79**, T63–T67 (1981).
51. Girdler, R. W. The measurement and computation of anisotropy of magnetic susceptibility of rocks. *Geophys. J. Int.* **5**, 34–44 (1961).
52. Hood, L. L. & Artemieva, N. A. Antipodal effects of lunar basin-forming impacts: initial 3D simulations and comparisons with observations. *Icarus* **193**, 485–502 (2008).
53. Daily, W. D. & Dyal, P. Theories for the origin of lunar magnetism. *Phys. Earth Planet. Inter.* **20**, 255–270 (1979).
54. Dyal, P., Parkin, C. W. & Daily, W. D. Global lunar crust: electrical conductivity and thermoelectric origin of remanent magnetism. In *Proc. 8th Lunar Science Conference* (ed. Merrill, R. B.) 767–783 (Pergamon Press, 1977).
55. Takahashi, F., Tsunakawa, H., Shimizu, H., Shibuya, H. & Matsushima, M. Reorientation of the early lunar pole. *Nat. Geosci.* **7**, 409–412 (2014).
56. Runcorn, S. K. Lunar magnetism, polar displacements and primeval satellites in the Earth–Moon system. *Nature* **304**, 589–596 (1983).

## Acknowledgements

We acknowledge funding from the NASA Solar System Workings Program (grant no. NNX15AL62G) to B.P.W. and from the NASA Solar System Exploration Virtual Institute (grant no. NNA14AB01A) to B.P.W. Additional funding support is acknowledged from the Simons Foundation (grant no. 556352) to C.I.O.N. We thank CAPTEM for the loan of samples. We thank R. Wells for assistance with sample orientation and photogrammetry. We thank L. de Groot, B. de Groot and the Utrecht University glass workshop for assistance with building a customized sample-handling system for anisotropy measurements. We thank S. Stanley for helpful discussions on dynamo theory. We thank F. Vervelidou for independently verifying the paleomagnetic data analysis.

## Author contributions

C.I.O.N. and B.P.W. wrote the paper. B.P.W. and H.H.S. conceived the study. C.I.O.N., B.L.G., A.B. and J.S. collected the palaeomagnetic data. C.I.O.N., B.P.W. and B.L.G. analysed the data and reconstructed palaeogeographic sample orientations. A.S.P.R. conducted the impact simulations.

## Competing interests

The authors declare no competing interests.

## Additional information

**Extended data** is available for this paper at https://doi.org/10.1038/s41550-021-01469-y.

**Supplementary information** The online version contains supplementary material available at https://doi.org/10.1038/s41550-021-01469-y.

**Correspondence and requests for materials** should be addressed to Claire I. O. Nichols.

**Peer review information** *Nature Astronomy* thanks Beck Strauss, Romain Tartese and the other, anonymous, reviewer(s) for their contribution to the peer review of this work.

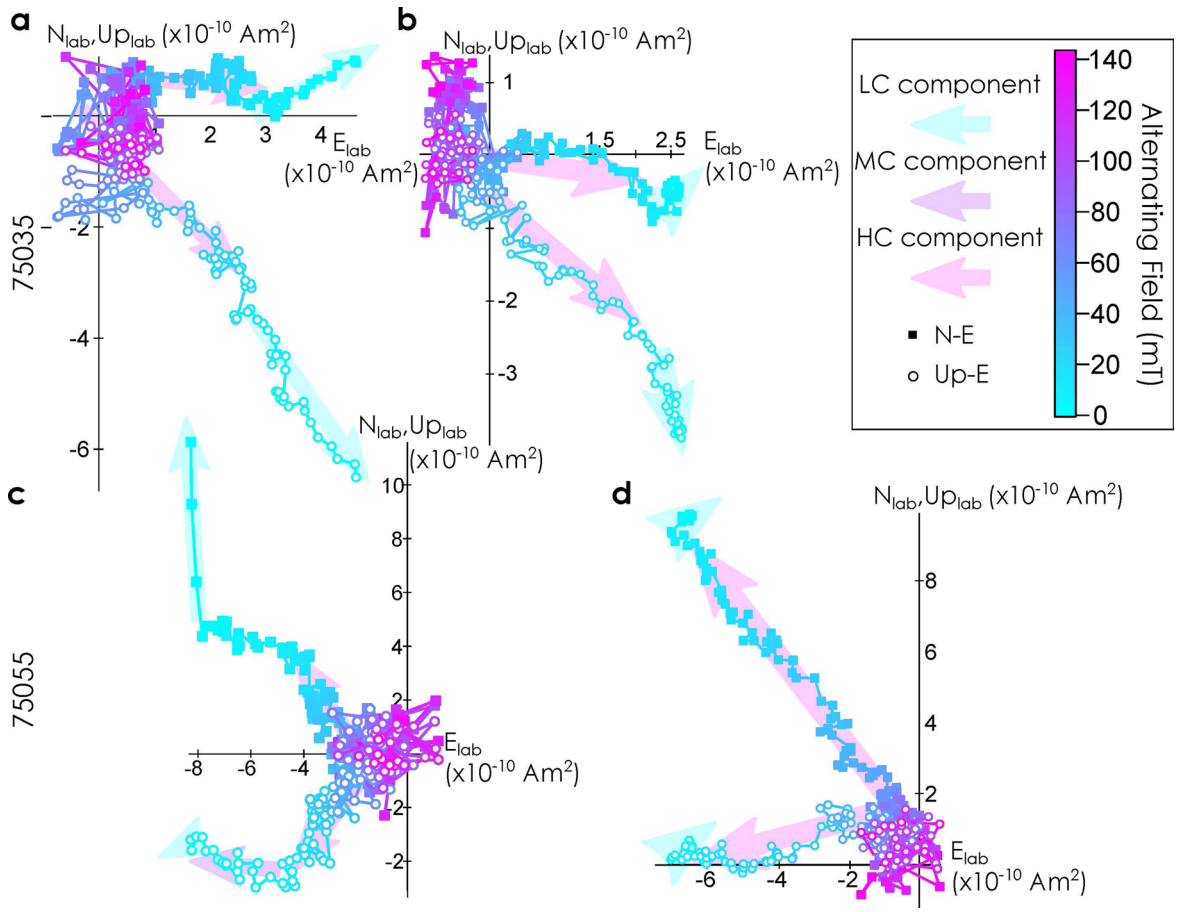


**Extended Data Fig. 1 | Demagnetization of NRM in 75035 and 75055.** Orthographic projections in laboratory coordinates (Table 1) show the nautral remanent magnetization (NRM) vector during alternating field demagnetization projected along the North-East (closed squares) and Up-East (open symbols) directions. Stable components are shown by blue (low coercivity, LC), purple (medium coercivity, MC) and red (high coercivity, HC) arrows, respectively. Data shown here are not corrected for remanence anisotropy. The peak AF is shown by the colour bar. **a**, Specimen 75035,242Ae. **b**, Specimen 75035,242Bg. **c**, Specimen 75055,127Aa. **d**, Specimen 75055,127Ae.

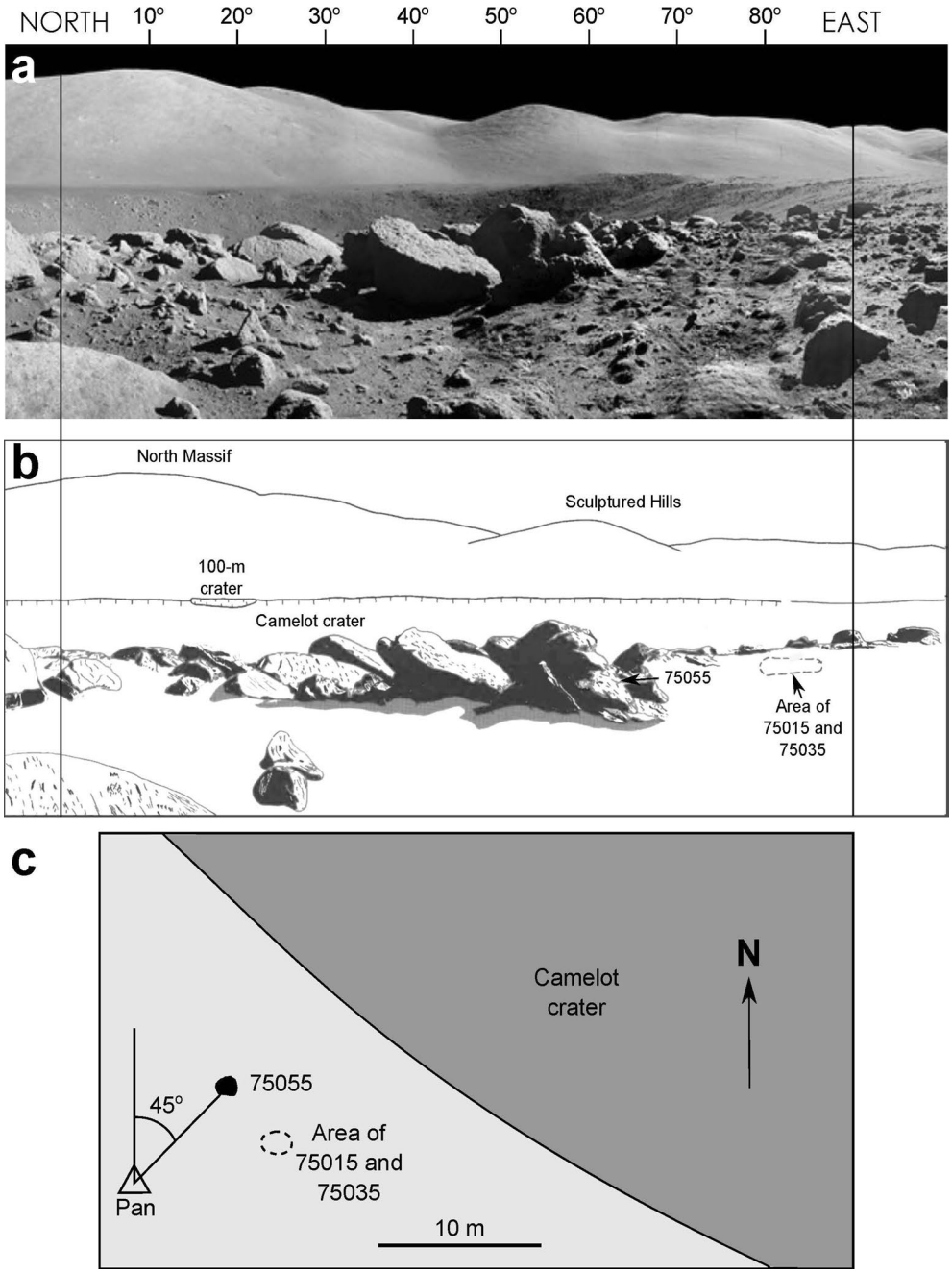


**Extended Data Fig. 2 | Geographic context of Station 5 where samples 75035 and 75055 were collected.** Figure adapted from ref. [25]. (a) Panorama 19 from ref. [25] using astronaut photographs AS17-145-22181, 22183, 22159 and 22160. The panorama shows a north-east view of the Taurus-Littrow valley. (b) Sketch corresponding to the panoramic photograph in (a). The locations of 75035 and 75055 are shown. (c) Map showing the location from which the panorama was taken and the position of 75035 and 75055 relative to Camelot crater.

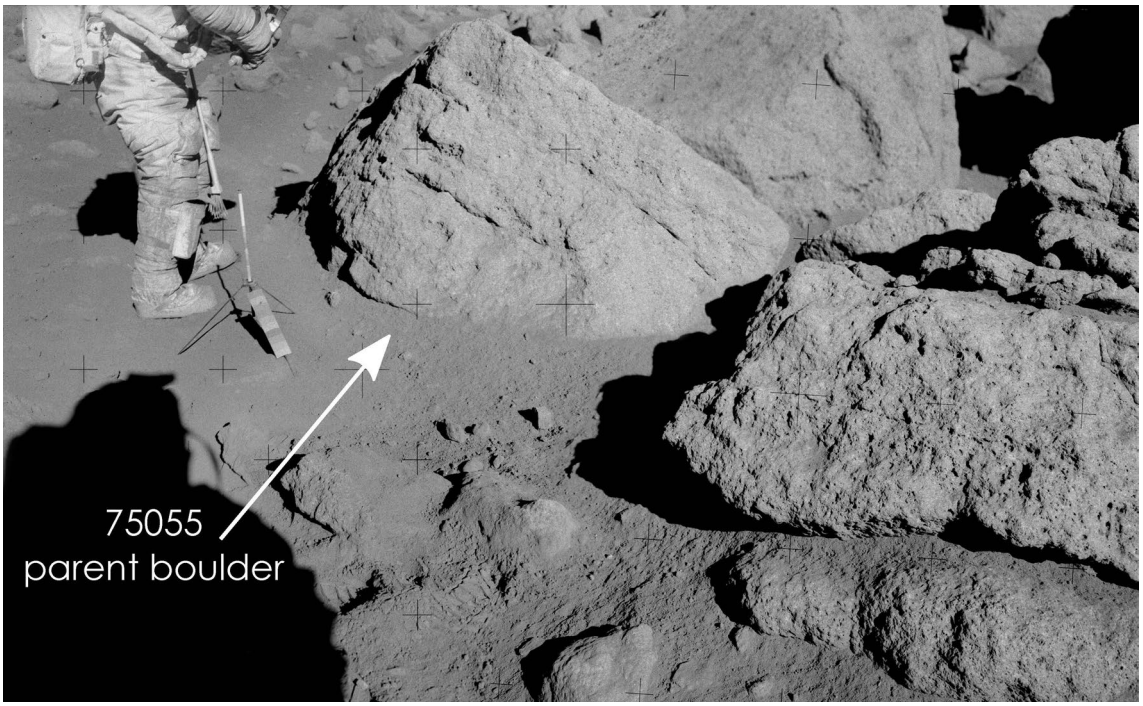


**Extended Data Fig. 3 | An example of the planar features in large blocks around Camelot Crater that were used to infer paleohorizontal.** Panorama using astronaut photographs AS17-133-20330 to AS17-133-20335. Astronaut E.A. Cernan is standing next to the block from which 75055 was sampled.

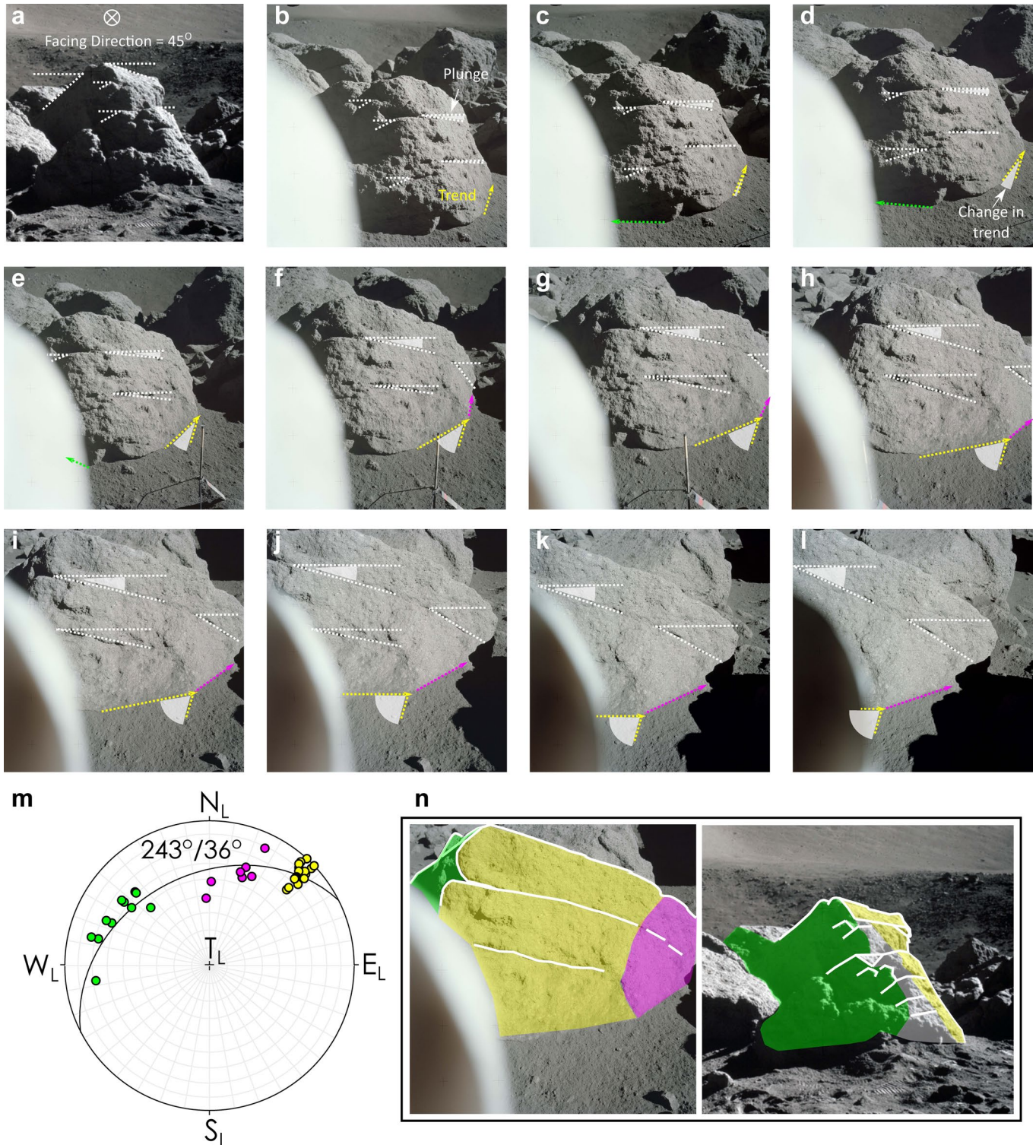


**Extended Data Fig. 4 | Estimation of the orientation of planar lava flow features on the 75055 parent boulder.** Measurements are summarized in Table S2. (a) Astronaut photograph AS17-145-22183. (b) - (l) Astronaut photographs AS17-145-22141 to AS17-145-22151 taken from a variety of orientations around the block. The trends and plunges of the planar features were measured as shown by the marked reference features. The colour of the trend arrow corresponds to the face on which the linear features were measured. (m) Equal area stereographic projection showing the orientation of the planar features with a strike and dip of 243°/36°. The plane of best fit was calculated from the measured trends and plunges of linear features identified on three faces of the boulder, coloured green, yellow and pink. (n) Annotated copies of (a) and (g) show the three faces identified on the boulder identified by the green, yellow and pink colours.

nature portfolio

https://doi.org/10.1038/s41550-021-01469-y

# Supplementary information

# The palaeoinclination of the ancient lunar magnetic field from an Apollo 17 basalt

In the format provided by the authors and unedited

# Supplementary Material: The Paleoinclination of the Ancient Lunar Magnetic Field from an Apollo 17 Basalt

Claire I. O. Nichols[a,b]*, Benjamin P. Weiss[a], Brenna L. Getzin[a], Harrison H. Schmitt[c], Annemarieke Béguin[d], Auriol S.P. Rae[e,f], Jay Shah[a]

*Corresponding author: claire.nichols@earth.ox.ac.uk

[a] Department of Earth, Atmospheric and Planetary Sciences, Massachusetts Institute of Technology, 77 Massachusetts Avenue, Cambridge, MA 02139, USA

[b] Now at: Department of Earth Sciences, University of Oxford, South Parks Road, Oxford, OX1 3AN, UK

[c] Department of Engineering Physics, University of Wisconsin-Madison, P.O. Box 90730, Albuquerque, NM 87199-0730, USA

[d] Paleomagnetic laboratory Fort Hoofddijk, Department of Earth Sciences, Utrecht University, Budapestlaan 17, 3584 CD Utrecht, The Netherlands

[e] Institute of Earth and Environmental Sciences – Geology, Albert-Ludwigs Universiät Freiburg, Albertstrasse 23b, 79104 Freiburg, Germany

[f] Department of Earth Sciences, University of Cambridge, Downing Street, Cambridge, CB2 3EQ, UK

# S1 Samples and Methods

## S1.1 Sample characterisation and preparation

Samples 75035 and 75055 are coarse-grained (typical silicate grain size of 1-2 mm), subophitic, high-Ti ilmenite basalts. They are of chemical type A and textural type 1B[11], which are thought to have formed as a result of a higher degree of chemical and mineralogical fractionation relative to other Apollo 17 basalts[12,13]. Sample 75035 has an integrated $^{40}Ar/^{39}Ar$ age of 3720 ± 40 Ma and a Rb-Sr age of 3750 ± 120 Ma[14,15], while sample 75055 has an integrated $^{40}Ar/^{39}Ar$ of 3760 ± 50 Ma and a Rb-Sr age of 3690 ± 70 Ma (indistinguishable from those of 75035)[14,16]. Recently, more precise Pb-Pb ages for 75035 and 75055 have yielded still-indistinguishable ages of 3753 ± 9 Ma and 3752 ± 9 Ma, respectively[17].

Electron microscopy data indicate samples 75035 and 75055 contain essentially pure-Fe kamacite ($\alpha$-Fe) with a dominantly multidomain grain size. However, isothermal remanent magnetization (IRM) acquisition data indicate 75035 and 75055 contain grains with coercivites $> 1000$ mT and $> 400$ mT, respectively, indicating the presence of a population of pseudo-single domain (e.g., single vortex) grains. Both 75035 and 75055 have cooling rates $< 3$ °C hr$^{-1}$ constrained by their petrographic textures[13,18], and therefore cooled too slowly to have recorded putative plasma fields or impact fields, which would have had a maximum duration of $< 1$ day. Additionally, neither sample exhibits evidence for shock metamorphism[19,20], indicating they never experienced a pressure wave with an amplitude greater than $\sim 5$ GPa (the Hugoniot elastic limit for lunar rocks[21,22]) and are unlikely to have acquired substantial shock remanent magnetization. The samples should therefore primarily contain a thermoremanent magnetization (TRM) acquired during primary cooling on the Moon after their emplacement.

We analysed subsamples 75035,242 and 75055,127, which B.P. Weiss and H.H. Schmitt acquired from JSC in 2016 (Figures S5 and S6). Sample 75035,242 was chipped from a slab that had previously been prepared using a bandsaw in 1973. Specimens 75035,242Ad and 75035,242Ah were immediately adjacent to the bandsaw cut and have been partially overprinted to coercivities $> 15$ mT (Figure S1). However, all other specimens were taken $> 2.5$ mm from the bandsaw cut and the overprint appears to have had no effect, which is consistent with the findings of ref. 23. Progressive AF applications revealed curved demagnetization trends for specimens 75035,242Ad and 75035,242Ah that we characterized be fitting approximate low coercivity (LC), medium coercivity (MC) and high coercivity (HC) components. The residual NRM direction progressively moved toward the HC component defined by pristine specimens, suggesting the bandsaw has only partially overprinted these specimens (Table S1 and Figure S1). This partial overprinting is consistent with previous paleomagnetic studies[23,24,25]. Sample 75055,127 was chipped from a slab (,1) that has never been bandsawn.

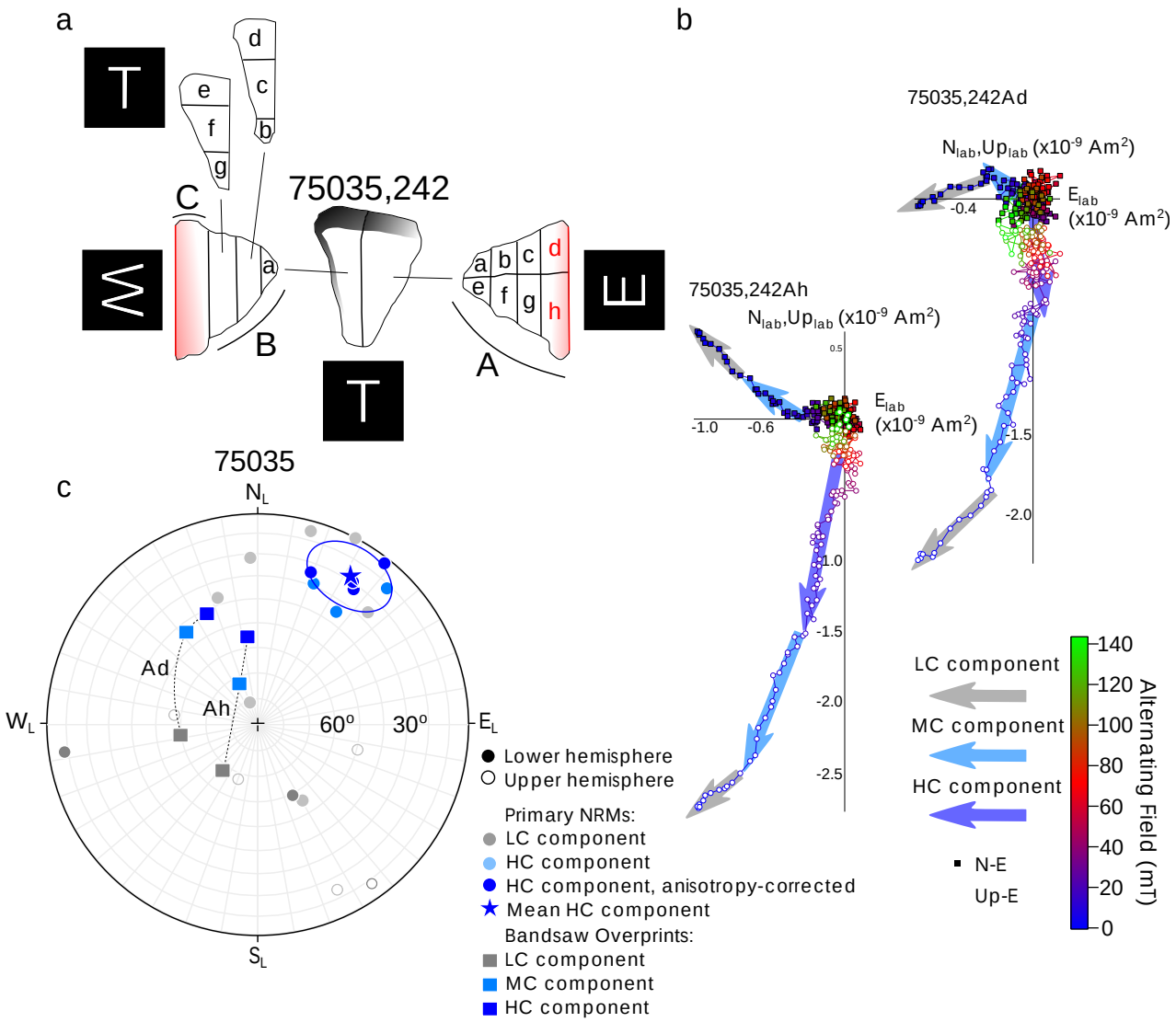


**Figure S1** | The influence of bandsaw cutting on the magnetization of specimens of 75035. Orientation cube is 1 cm across. (a) Diagram showing from where each of our specimens was taken relative to the bandsaw cut. (b) Orthographic projections in laboratory coordinates showing the NRM vector during AF demagnetization for 75035,242Ad and 75035,242Ah in three components projected along the North-East (closed squares) and Up-East (open symbols) directions. Stable components are shown by grey (LC), light blue (medium coercivity, MC) and bright blue (HC) arrows, respectively. (c) Equal area stereographic projection showing the approximate LC, MC and HC components for each specimen of 75035 in lunar coordinates. The two specimens that were immediately adjacent to the bandsaw cut (75035,242Ad and 75035,242Ah) were partially overprinted by the bandsaw, as demonstrated by the fact that during AF demagnetization the NRM progressively moves towards the HC direction defined by the other specimens. All other specimens were acquired > 2.5 mm from the bandsaw cut and show no evidence of badsaw overprints.

| Sample | LC | | | MC | | | HC | | |
|---|---|---|---|---|---|---|---|---|---|
| | AF (mT) | Dec (°) | Inc (°) | AF (mT) | Dec (°) | Inc (°) | AF (mT) | Dec (°) | Inc (°) |
| 75035,242Ad | 0 – 7 | 245 | 42 | 7 – 17 | 298 | 71 | 17 – 28 | 324 | 78 |
| 75035,242Ah | 0 – 7 | 222 | 32 | 7 – 15 | 213 | 66 | 15 – 50 | 185 | 83 |

**Table S1** | LC, MC and HC components of magnetization for bandsaw-overprinted samples 75035,242Ad and 75035,242Ah in laboratory coordinates. The first, second, third and fourth columns list the sample name, AF range, declination and inclination of the LC component, respectively. The fifth, sixth and seventh columns list the AF range, declination and inclination of the MC component, respectively. The eight, ninth and tenth columns list the AF range, declination and inclination of the HC component, respectively.

Further subsampling was then conducted in the MIT Paleomagnetism Laboratory using a diamond wire saw in a magnetically shielded clean room (DC field $< 200$ nT) to generate specimens for paleomagnetic analysis. Consistent orientations were maintained between all specimens using an orientation cube in laboratory coordinates. For 75035, this orientation system is distinct from JSC coordinates, whereas for 75055, laboratory and JSC coordinates are the same (Table 1). For both samples, the JSC orientation system is distinct from that of present-day lunar geographic coordinates (Table 1). Each specimen was mounted on a 2.5-cm-diameter quartz disc with a magnetic moment $< 2 \times 10^{-12}$ Am$^2$ using a small quantity of cyanoacrylate cement. Specimens were mounted in different orientations relative to one another to ensure there is no directional bias induced by the measurement procedure.

In addition to our measurements, previously-measured hysteresis properties of both 75035 and 75055 indicate a dominantly multidomain state[26]. Previous paleomagnetic studies have reported stable (up to a 1 hour unblocking temperature of $\sim 200$ °C[27] and a peak alternating field (AF) $\sim 11$ mT[5]) natural remanent magnetization (NRM) in both samples. An NRM component was identified in 75035[27] , but it was unclear whether this was a primary TRM or a secondary overprint[28]. A previous study of 75055 yielded a paleointensity of $\sim 84$ $\mu$T using anhysteretic remanent magnetization (ARM) paleointensity methods on a single large (374 mg) sample[5]. In this study, we have improved constraints on the recovered paleointensity for 75055 through measurements of multiple specimens.

Two previous paleomagnetic studies of Apollo samples have attempted to constrain the paleodirection of the lunar magnetic field[5,29]. One study of mare basalts tentatively suggested that the lunar dynamo 3.3 – 3.8 Ga ago was dipolar and aligned along the present-day spin axis[5]. The other study[29] was conducted on regolith breccia 15015, but the stable magnetization in this sample has subsequently been shown to have been produced during saw cutting at the Johnson Space Center (JSC)[23].

## S1.2 Orienting samples in lunar coordinates

To translate samples from one coordinate system to another, a series of rotations are made which can also be described by a single $3 \times 3$ matrix. The rotations and associated translation matrices are shown in Figures S2, S3 and S4. The translation matrices $\mathbf{A_{JSC}}$ and $\mathbf{A_L}$ are used to translate from laboratory to JSC and JSC to present-day lunar coordinates, respectively:

$$\begin{pmatrix} N \\ E \\ T \end{pmatrix}_{JSC} = \mathbf{A_{JSC}} \times \begin{pmatrix} N \\ E \\ T \end{pmatrix}_{lab} \tag{1}$$

$$\begin{pmatrix} N \\ E \\ T \end{pmatrix}_{L} = \mathbf{A_L} \times \begin{pmatrix} N \\ E \\ T \end{pmatrix}_{JSC} \tag{2}$$

The uncertainty associated with the rotations is difficult to quantify. However, we conservatively assume an uncertainty of 5° for each rotation. Summing these uncertainties in quadrature, the maximum uncertainty in rotating 75035 from lab to JSC coordinates (3 rotations) is 9°. The maximum uncertainty in rotating 75035 from JSC to lunar coordinates (4 rotations) is 10°. The maximum uncertainty in rotating 75055 from JSC to lunar coordinates (five rotations) is 11°, and the uncertainty on the tilt correction to lunar paleohorizontal is 5°. Therefore the total uncertainty in orienting samples 75035 and 75055 is 13° and 12°, respectively. Because of the ambiguities with estimating these orientation uncertainties, our interpretations of the paleoinclination of the lunar dynamo from sample 75055 in the Main Text only include the uncertainty from paleomagnetic analysis ($\alpha_{95} = 10°$). Taking into account the additional uncertainty from rotations gives a paleoinclination estimate of 34 ± 16°.

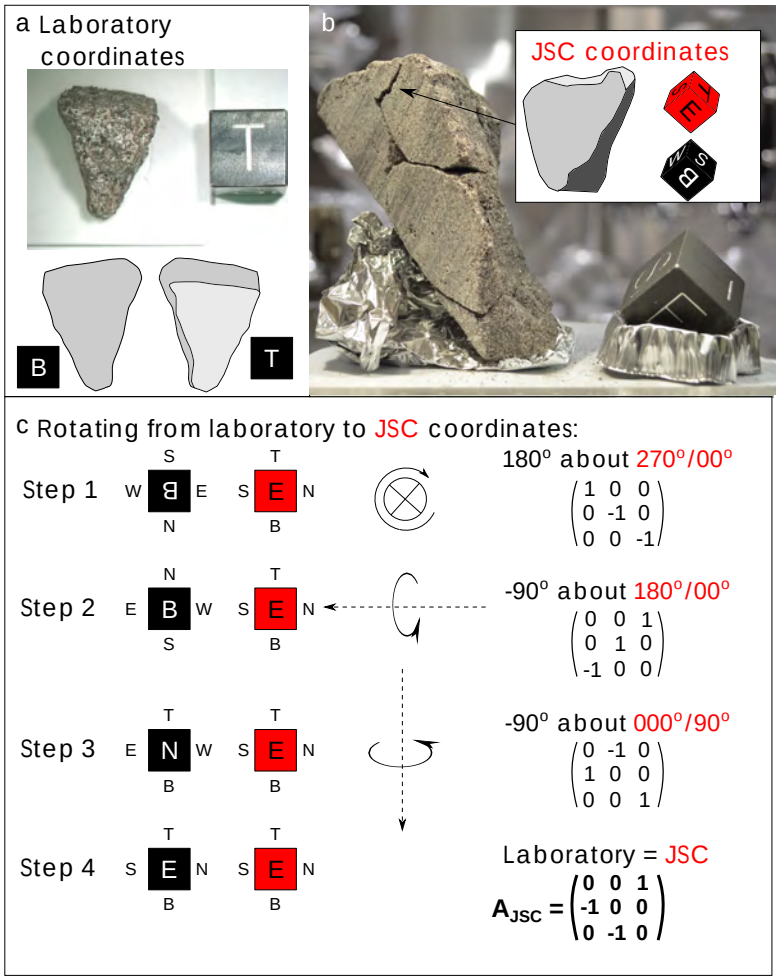


**Figure S2** | The four steps to rotate subsample 75035,242 from its orientation in the MIT Paleomagnetism Laboratory to JSC coordinates. Rotations are referenced to the JSC coordinate reference frame. (a) The orientation of the subsample in the MIT Paleomagnetism Laboratory. (b) The orientation of the subsample photographed at the JSC. Note JSC bandsaw surface on the southeast face of the sample. (c) The steps required to rotate from laboratory to JSC coordinates. Laboratory orientation is shown by the black cube and JSC orientation by the red cube throughout. The rotation matrix is shown for each step. The rotation matrix to transform directly from laboratory to JSC coordinates is shown in bold.

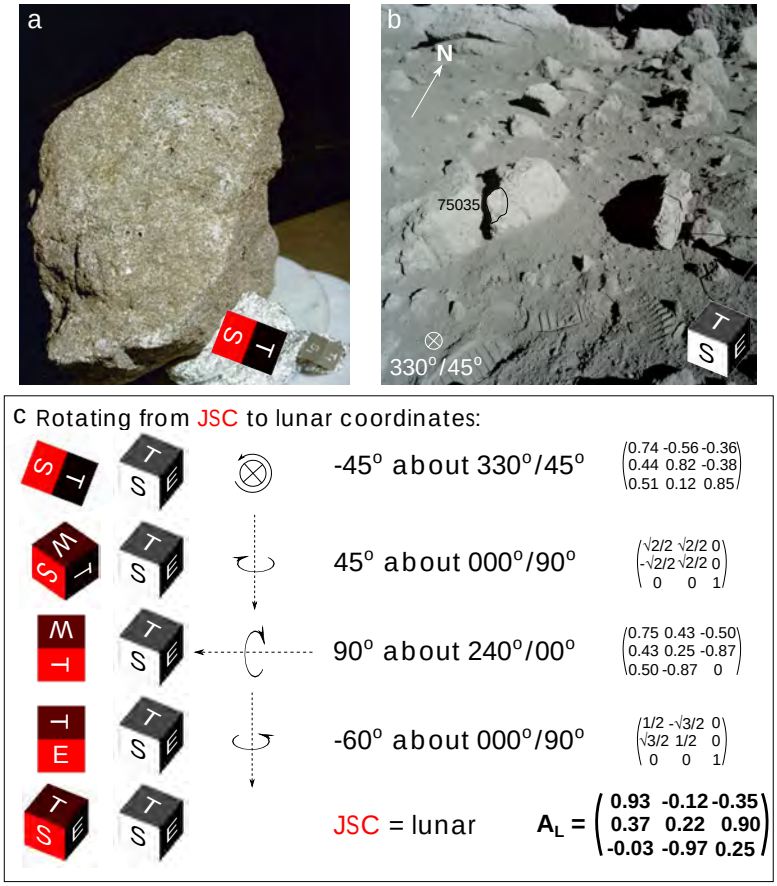


**Figure S3** | The steps to rotate sample 75035 from JSC to lunar coordinates. Rotations are made in the lunar coordinate reference frame. (a) JSC photograph S73-19593 showing the orientation of 75035 in JSC coordinates. The sample was illuminated under the same light conditions as those when it was sampled on the Moon. (b) Astronaut photograph AS17-145-22138 showing the orientation of 75035 in lunar coordinates. The direction of North is taken from ref. 30. (c) The steps required to rotate from JSC to lunar coordinates. JSC orientation is shown by the red cube and lunar orientation by the white cube throughout. The rotation matrix is shown for each step. The rotation matrix to transform directly from JSC to lunar coordinates is shown in bold.

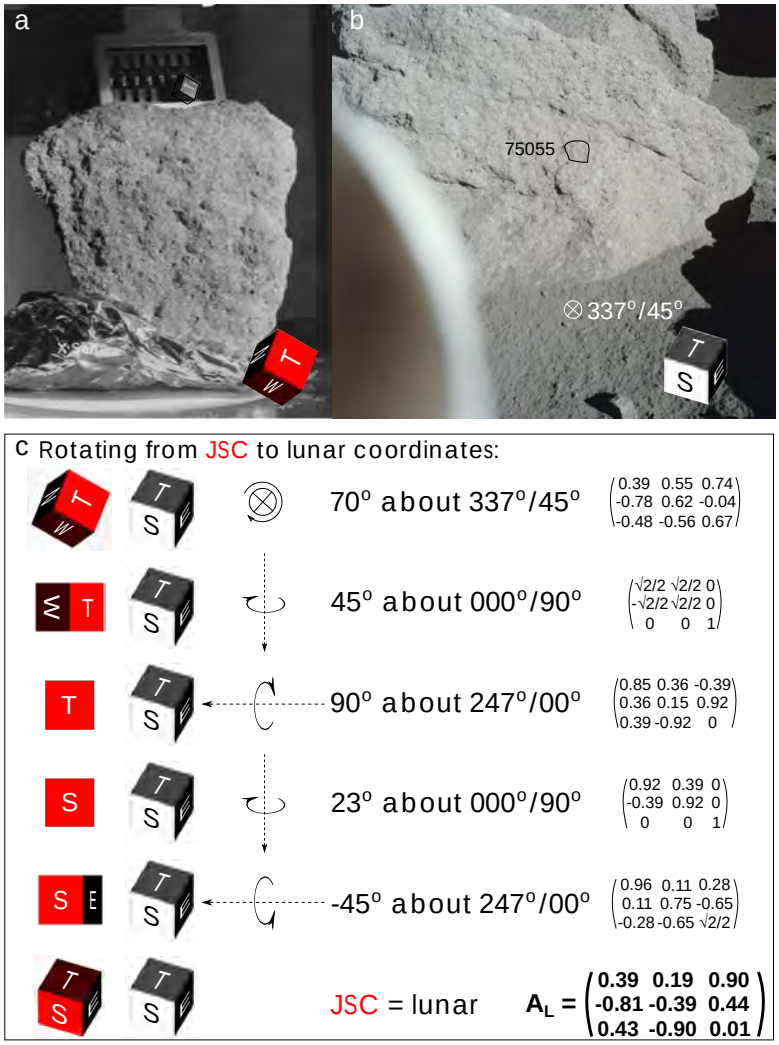


**Figure S4** | The steps to rotate sample 75055 from JSC to lunar coordinates. Rotations are made in the lunar coordinate reference frame. (a) JSC photograph S73-17796 showing the orientation of 75055 in JSC coordinates. (b) Astronaut photograph AS17-145-22149 showing the orientation of 75055 in lunar coordinates. The direction of the photograph was determined from the change in trend from Astronaut photograph AS17-145-22141 (see Extended Data figures 2 and 4). (c) The steps required to rotate from JSC to lunar coordinates. JSC orientation is shown by the red cube and lunar orientation by the white cube throughout. The rotation matrix is shown for each step. The rotation matrix to transform directly from JSC to lunar coordinates is shown in bold.

| Figure | Photograph | Direction of Facing (°) | Change in Trend (°) | Plunge (°) | Trend (°) |
|---|---|---|---|---|---|
| a | 22183 | 45 | 0 | 42 | 315 |
| a | 22183 | 45 | 0 | 28 | 315 |
| a | 22183 | 45 | 0 | 29 | 315 |
| a | 22183 | 45 | 0 | 17 | 45 |
| a | 22183 | 45 | 0 | 26 | 45 |
| b | 22141 | 30 | 15 | 9 | 46 |
| b | 22141 | 30 | 15 | 33 | 307 |
| b | 22141 | 30 | 15 | 27 | 307 |
| b | 22141 | 30 | 15 | 25 | 307 |
| b | 22141 | 30 | 15 | 3 | 46 |
| c | 22142 | 22 | 23 | 9 | 42 |
| c | 22142 | 22 | 23 | 27 | 294 |
| c | 22142 | 22 | 23 | 23 | 294 |
| c | 22142 | 22 | 23 | 0 | 42 |
| d | 22143 | 10 | 43 | 9 | 46 |
| d | 22143 | 10 | 43 | 0 | 46 |
| d | 22143 | 10 | 43 | 22 | 284 |
| d | 22143 | 10 | 43 | 17 | 284 |
| e | 22144 | 356 | 49 | 5 | 41 |
| e | 22144 | 356 | 49 | 22 | 263 |
| e | 22144 | 356 | 49 | 7 | 41 |
| f | 22145 | 345 | 60 | 12 | 45 |
| f | 22145 | 345 | 60 | 8 | 45 |
| f | 22145 | 345 | 60 | 51 | 357 |
| g | 22146 | 337 | 68 | 11 | 43 |
| g | 22146 | 337 | 68 | 11 | 43 |
| g | 22146 | 337 | 68 | 41 | 1 |
| h | 22147 | 329 | 76 | 12 | 47 |
| h | 22147 | 329 | 76 | 12 | 47 |
| h | 22147 | 329 | 76 | 32 | 18 |
| i | 22148 | 326 | 79 | 15 | 44 |
| i | 22148 | 326 | 79 | 16 | 44 |
| i | 22148 | 326 | 79 | 35 | 20 |
| j | 22149 | 317 | 88 | 18 | 47 |
| j | 22149 | 317 | 88 | 28 | 20 |
| k | 22150 | 315 | 90 | 24 | 45 |
| k | 22150 | 315 | 90 | 32 | 18 |
| l | 22151 | 314 | 91 | 17 | 44 |
| l | 22151 | 314 | 91 | 32 | 25 |
| l | 22151 | 314 | 91 | 11 | 25 |

**Table S2** | Measurements corresponding to Extended Data figure 4 for determining the strike and dip of planar features observed on the 75055 parent boulder. The first column lists the part of the figure to which the measurements correspond. The second column lists the astronaut photograph number (each preceded by "AS17-254-"). The third column lists the facing direction (i.e., the direction toward which the astronaut took the photograph). The fourth column lists the change in orientation between the photograph and photograph AS17-145-22183 determined using linear features. The fifth column lists the plunge, which is the angle between horizontal and the linear features from the perspective of each photograph. The sixth column lists the apparent trend of the linear features from the perspective of the facing direction.

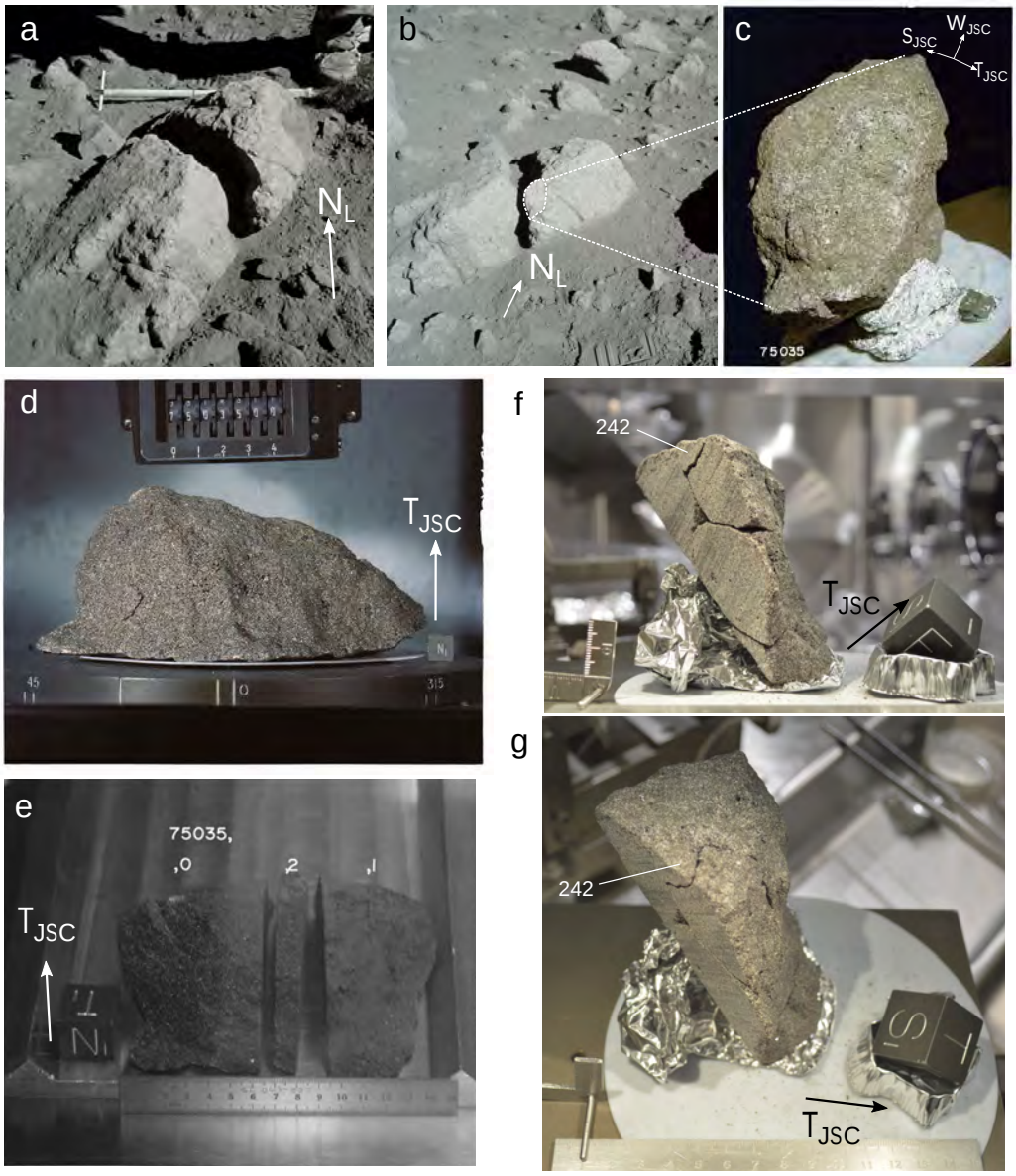


**Figure S5** | The location of sample 75035 on the lunar surface and subsequent orientation and sampling at JSC. (a) Astronaut photograph AS17-145-22139 showing the location of 75035 prior to sampling from the boulder on the lunar surface. 61-cm-long hammer for scale. (b) Astronaut photograph AS17-145-22138 showing the side of the boulder and location of 75035 prior to sampling. (c) JSC photograph S73-19593 showing 75035 in JSC coordinates photographed in the same orientation and lighting conditions as when sampled on the Moon. (d) JSC photograph S73-24259 of the north face of 75035 (in JSC coordinates prior to cutting or chipping). The sample cube is 1 cm across. (e) Photograph S73-31658 showing slabbing of 75035 into three slabs 75035,0, 75035,1 and 75035,2. Slabbing was carried out using the JSC bandsaw. Subsample 75035,242 is part of 75035,1. The orientation cube is 2.5 cm across. (f) Photograph taken during sampling by B.P. Weiss and H.H. Schmitt in 2016 at JSC. Location of sample 75035,242 from cut face (east relative to 2.5 cm orientation cube). (g) Photograph taken during sampling by B.P. Weiss and H.H. Schmitt in 2016 at JSC. Location of sample 75035,242 from the top (south relative to 2.5 cm orientation cube).

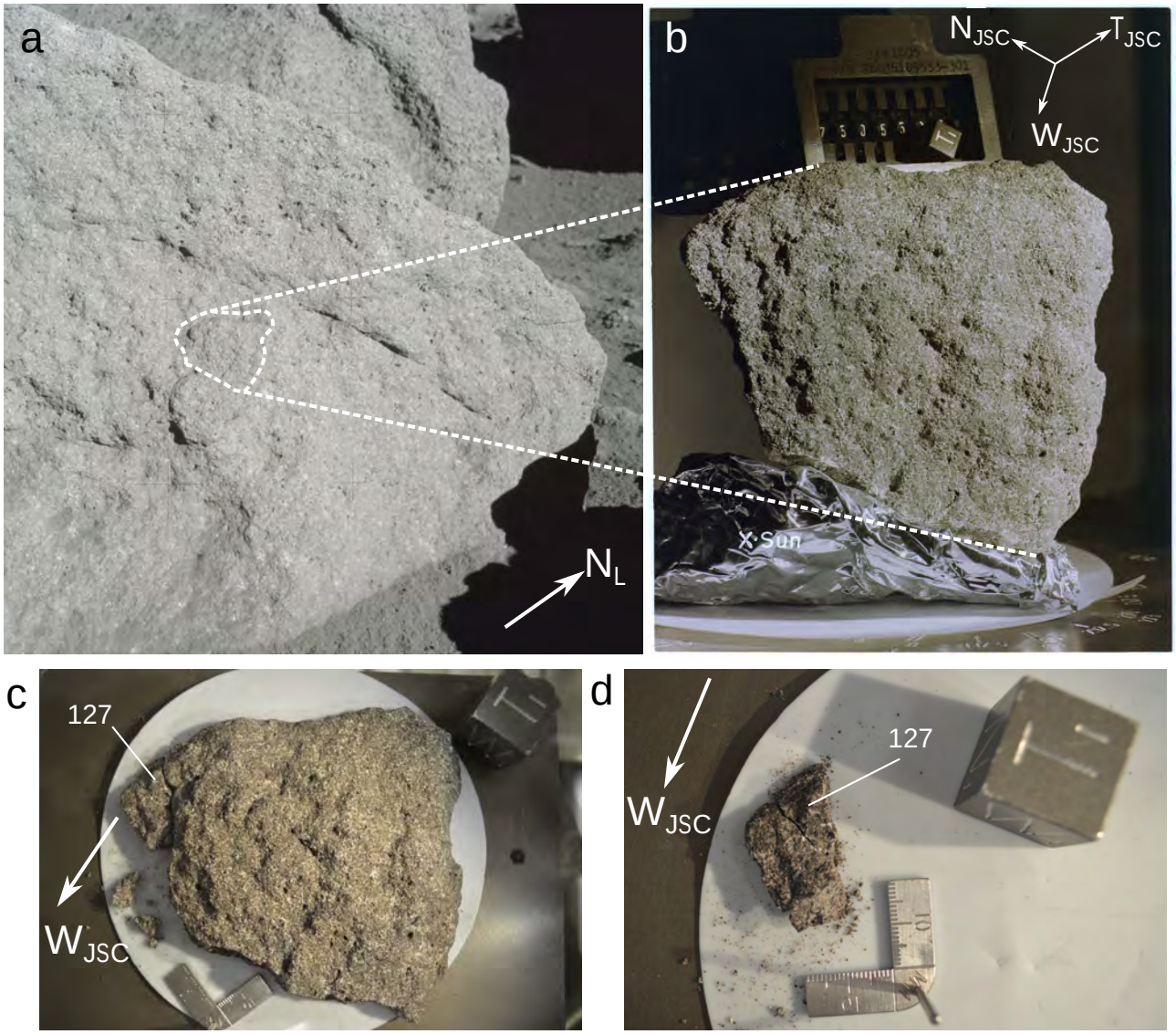


**Figure S6** | The location of sample 75055 on the lunar surface and subsequent orientation and sampling of subsample 75055,127 at JSC. (a) Astronaut photograph AS17-145-22149 showing the location of 75055 prior to sampling from the boulder on the lunar surface. (b) JSC photograph S73-17796 showing the top face of 75055 (in JSC coordinates) prior to chipping. The sample is photographed in the same orientation and lighting conditions as when sampled on the Moon. The sample cube is 1 cm across. (c) Photograph taken during sampling by B.P. Weiss and H.H. Schmitt in 2016 at JSC. Sample 75055 was chipped into smaller fragments. Subsample 75055,127 is in the upper left of the photo. The orientation cube is 2.5 cm across. (d) Photograph taken during sampling by B. Weiss and H. Schmitt in 2016 at JSC. The relative orientation of subsample 75055,127 to 75055,128 and the orientation cube (2.5 cm across).

## S1.3 Petrographic analysis

Plagioclase crystals typically define lineations corresponding to flow directions within bodies of magma; the average lineation typically lies approximately in the paleohorizontal plane[31,32]. In an attempt to identify such lineation in our samples as an independent indicator of paleohorizontality, we analysed 30-$\mu$m thin sections 75035,84 and 75055,46 in plane-polarized and cross-polarized transmitted light. Plagioclase crystals were used to assess the degree of flow alignment, since they have the most elongate morphology and their orientation can easily be constrained parallel to the direction of twinning. A histogram of directions was calculated to determine the degree of alignment of plagioclase crystals using the directionality package in the imaging software Fiji (ImageJ)[33,34]. Crystal orientations were grouped in 10° bins.

We analysed the same thin sections using backscattered electron microscopy (BSEM). Samples were carbon coated and imaged at the MIT Electron Microprobe Facility using a JEOL-JXA-8200 electron microprobe. Mineral compositions were assessed using wavelength dispersive spectroscopy (WDS) for Fe, Ni and S (Table S3).

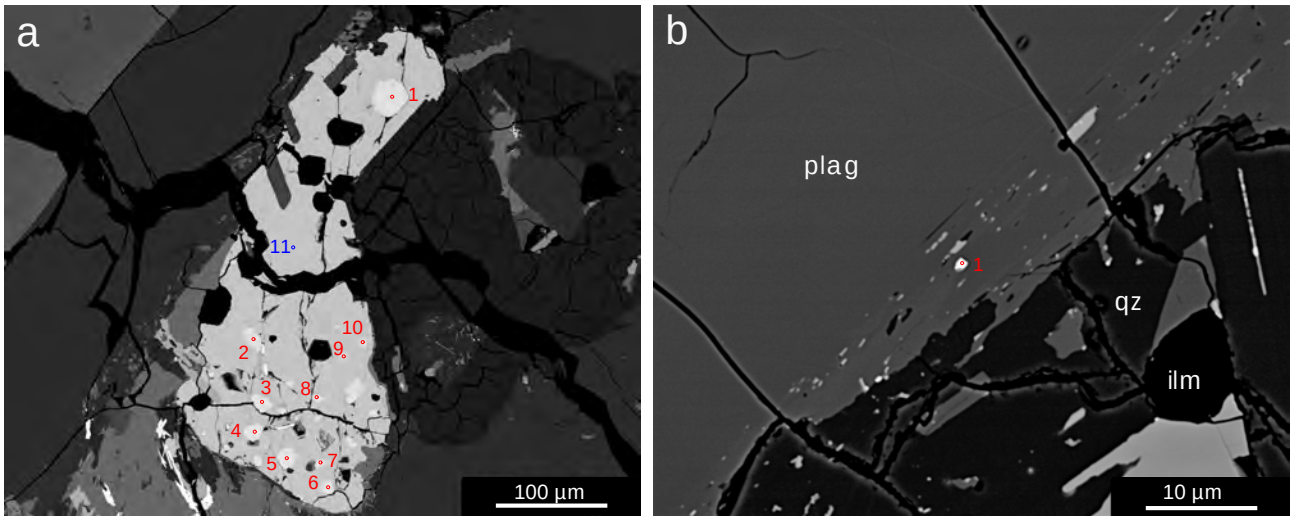


**Figure S7** | BSEM images of 75035. Red (kamacite) and blue (troilite) circles/numbers show locations of WDS probe measurements (Table S3). (a) Pure Fe kamacite blebs within troilite. (b) Pure Fe kamacite bleb within a crystal of plagioclase. plag = plagioclase, qz = quartz, ilm = ilmenite.

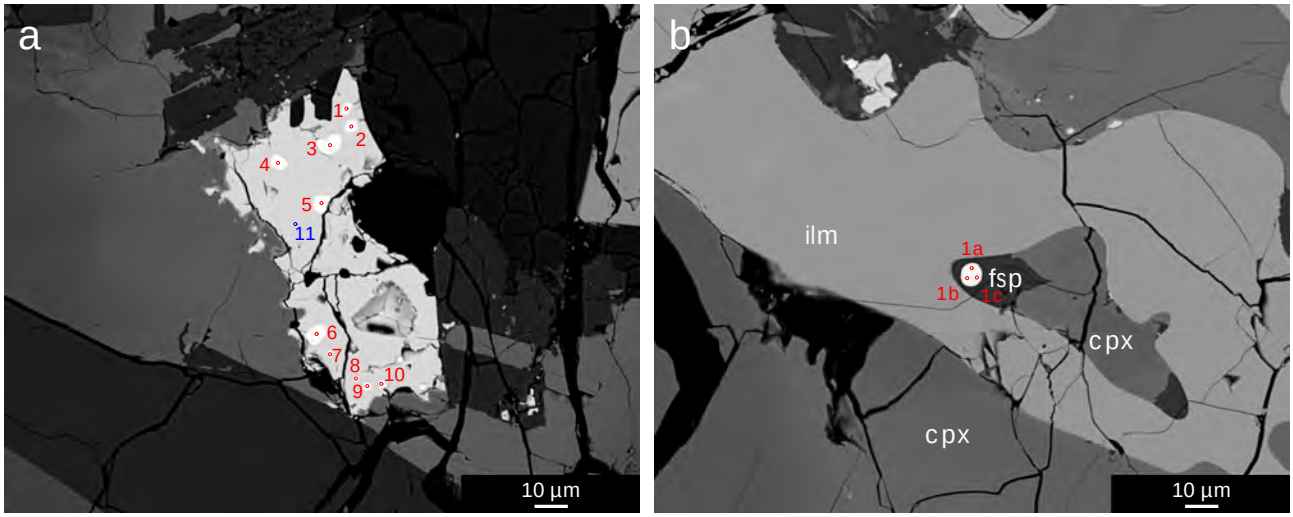


**Figure S8** | BSEM images of 75055. Red (kamacite) and blue (troilite) circles/numbers show the locations of WDS probe measurements (Table S3). (a) Pure Fe kamacite blebs within troilite. (b) Pure Fe kamacite bleb within a crystal of feldspar. ilm = ilmenite, cpx = clinopyroxene, K-fsp = feldspar.

| | | 75035 | | | | | | 75055 | | | |
|---|---|---|---|---|---|---|---|---|---|---|---|
| Figure | Point | Fe (wt%) | Ni (wt%) | S (wt%) | Mineral | Figure | Point | Fe (wt%) | Ni (wt%) | S (wt%) | Mineral |
| S7a | 1 | 100.00 | 0.00 | 0.00 | kamacite | S8a | 1 | 100.00 | 0.00 | 0.00 | kamacite |
| S7a | 2 | 100.00 | 0.00 | 0.00 | kamacite | S8a | 2 | 100.00 | 0.00 | 0.00 | kamacite |
| S7a | 3 | 100.00 | 0.00 | 0.00 | kamacite | S8a | 3 | 100.00 | 0.00 | 0.00 | kamacite |
| S7a | 4 | 100.00 | 0.00 | 0.00 | kamacite | S8a | 4 | 100.00 | 0.00 | 0.00 | kamacite |
| S7a | 5 | 100.00 | 0.00 | 0.00 | kamacite | S8a | 5 | 100.00 | 0.00 | 0.00 | kamacite |
| S7a | 6 | 99.99 | 0.01 | 0.00 | kamacite | S8a | 6 | 100.00 | 0.00 | 0.00 | kamacite |
| S7a | 7 | 100.00 | 0.00 | 0.00 | kamacite | S8a | 7 | 100.00 | 0.00 | 0.00 | kamacite |
| S7a | 8 | 100.00 | 0.00 | 0.00 | kamacite | S8a | 8 | 100.00 | 0.00 | 0.00 | kamacite |
| S7a | 9 | 100.00 | 0.00 | 0.00 | kamacite | S8a | 9 | 100.00 | 0.00 | 0.00 | kamacite |
| S7a | 10 | 99.99 | 0.01 | 0.00 | kamacite | S8a | 10 | 100.00 | 0.00 | 0.00 | kamacite |
| S7a | 11 | 62.38 | 0.00 | 37.62 | troilite | S8a | 11 | 62.50 | 0.00 | 37.50 | troilite |
| S7b | 1 | 100.00 | 0.00 | 0.00 | kamacite | S8b | 1a | 100.00 | 0.00 | 0.00 | kamacite |
| | | | | | | S8b | 1b | 100.00 | 0.00 | 0.00 | kamacite |
| | | | | | | S8b | 1c | 100.00 | 0.00 | 0.00 | kamacite |

**Table S3** | WDS data for analyses of BSEM images shown in Figures S7 and S8. The first and seventh columns correspond to the figure showing the location of each probe measurement for 75035 and 75055, respectively. The second and eighth columns correspond to the specific probe point for 75035 and 75055, respectively. The third and ninth columns list the Fe content, the fourth and tenth columns list the Ni content and the fifth and eleventh columns list the S content measured using WDS for 75035 and 75055 respectively. The sixth and twelfth columns list the mineral.

## S2 Results

### S2.1 Magnetic Carriers

The ferromagnetic carriers in 75035 and 75055 are kamacite inclusions located in troilite and silicate minerals (e.g., plagioclase and feldspar) (Figures S7 and S8). WDS measurements of the inclusions show that the kamacite is 100 wt. % Fe. BSEM images show that the largest inclusions are $\sim 1 - 10$ $\mu$m in diameter and have an equant morphology, suggesting they are multidomain[35]. Curie balance analysis showed that during heating of specimen 75055,127Ac the magnetization decayed as it approached 700 °C, consistent with kamacite as the primary magnetic carrier. IRM acquisition suggest grains have coercivities extending to $> 1000$ mT, indicative of a population of smaller, single to pseudo-single domain (e.g., vortex state) kamacite grains (Figure S11).

### S2.2 The paleomagnetic recording fidelity of samples 75035 and 75055

Specimens were AF demagnetized because of the likelihood of alteration during thermal demagnetization due to the presence of troilite[36]. Susceptibility to thermal alteration was also confirmed by our Curie balance analysis on specimen 75055,127Ac (Figure S9), although this was expected since experiments were conducted in air. Upon cooling, the magnetization of specimen 75055,127Ac increases by a factor of 3 at room temperature relative to the magnetization prior to heating. Magnetization begins to increase below $\sim 580$ °C suggesting the formation of magnetite by thermal alteration. The overall increase in magnetization may be due to troilite alteration; since troilite is essentially non-magnetic, alteration to magnetite or iron will cause an increase in magnetic moment.

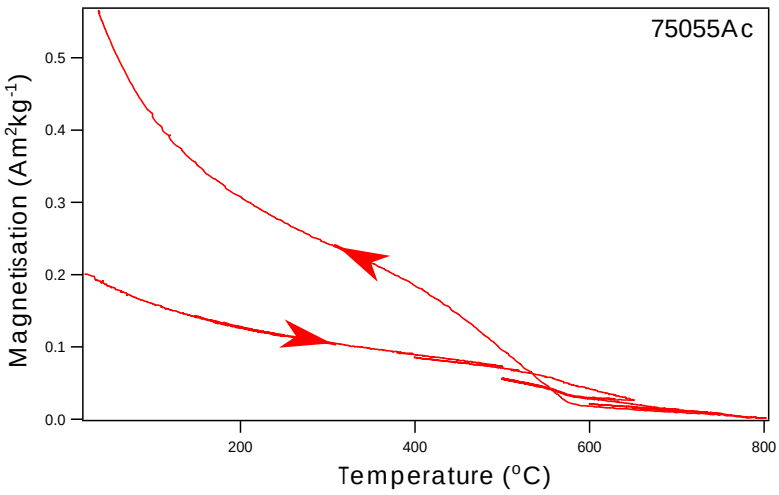


**Figure S9** | Curie balance data for specimen 75055,127Ac. During heating in air to 800 °C the sample loses magnetization at $> 700$ °C, consistent with the presence of kamacite. During cooling, the sample gains significantly more magnetization than it had prior to heating, particularly at $\sim 580$ °C, suggesting magnetite has formed during thermal alteration.

To assess the paleomagnetic fidelity of the samples, we used two metrics: difference $D'$ and error

$E$. A permissive threshold for reasonable paleomagnetic recording fidelity[37] is -50% $< D' <$ 100% and $E <$ 50%. The metrics for our specimens are summarized in Table S4. As expected, our ability o reliably retrieve a paleointensity diminishes with decreasing ARM strength. We found that we were able to consistently recover paleointensities of $<$ 7.5 $\mu$T from specimens of 75035 and $<$ 37.3 $\mu$T from specimens of 75055.

| Sample | ARM DC field ($\mu$T) | TRM Equivalent ($\mu$T) | Field Range (mT) | Retrieved Paleointensity ($\mu$T) | $E$ (%) | $D'$ (%) | Accepted |
|---|---|---|---|---|---|---|---|
| 75035,242Aa | 50 | 37.3 | 6.5 – 137.0 | 27.85 $\pm$ 4.19 | 11 | -25 | ✓ |
| 75035,242Af | 50 | 37.3 | 10.0 – 39.0 | 41.24 $\pm$ 3.43 | 9 | 11 | ✓ |
| | 20 | 14.9 | 10.0 – 39.0 | 14.4 $\pm$ 2.6 | 17 | -4 | ✓ |
| | 10 | 7.5 | 10.0 – 39.0 | 15.8 $\pm$ 2.3 | 31 | 112 | × |
| 75035,242Bc | 50 | 37.3 | 8.0 – 45.0 | 48.8 $\pm$ 3.4 | 9 | 31 | ✓ |
| | 30 | 22.4 | 8.0 – 45.0 | 27.3 $\pm$ 3.0 | 13 | 22 | ✓ |
| | 20 | 14.9 | 8.0 – 45.0 | 12.3 $\pm$ 3.2 | 21 | -18 | ✓ |
| | 10 | 7.5 | 8.0 – 45.0 | 13.9 $\pm$ 2.1 | 28 | 86 | ✓ |
| 75055,127a | 20 | 14.9 | 3.0 – 53.0 | 32.2 $\pm$ 5.6 | 38 | 116 | × |
| 75055,127b | 50 | 37.3 | 4.0 – 24.5 | 22.9 $\pm$ 5.3 | 14 | -39 | ✓ |
| | 34 | 25.4 | 7.0 – 24.5 | 8.5 $\pm$ 4.9 | 19 | -67 | × |
| | 10 | 7.5 | 7.5 – 24.5 | 3.8 $\pm$ 5.4 | 72 | -49 | ✓ |
| | 5 | 3.7 | 4.0 – 24.5 | 1.0 $\pm$ 4.9 | 131 | -73 | × |
| 75055,127c1 | 50 | 37.3 | 0.0 – 50.0 | 39.9 $\pm$ 2.1 | 6 | 7 | ✓ |
| 75055,127c2 | 50 | 37.3 | 3.5 – 15.5 | 24.5 $\pm$ 3.1 | 8 | -34 | ✓ |
| 75055,127Aa | 50 | 37.3 | 9.0 – 34.0 | 34.3 $\pm$ 3.9 | 10 | -8 | ✓ |
| 75055,127Ab | 50 | 37.3 | 4.5 – 20.0 | 33.8 $\pm$ 4.5 | 12 | -9 | ✓ |
| 75055,127Ae | 50 | 37.3 | 7.5 – 28.0 | 46.1 $\pm$ 5.7 | 15 | 24 | ✓ |

**Table S4** | Paleointensity fidelity tests for 75035 and 75055. The first column lists the specimens. The second column lists the DC bias field used to impart an ARM. The third column lists the TRM-equivalent field using $f'$ = 1.34. The fourth column lists the field range over which the paleointensity estimate was calculated. The fifth column lists the paleointensity calculated using the ARM paleointensity method. The sixth column lists the ratio error metric, $E$. The seventh column lists the difference metric, $D'$. The eighth column lists whether the specimen passes the acceptance criteria defined by ref. 37.

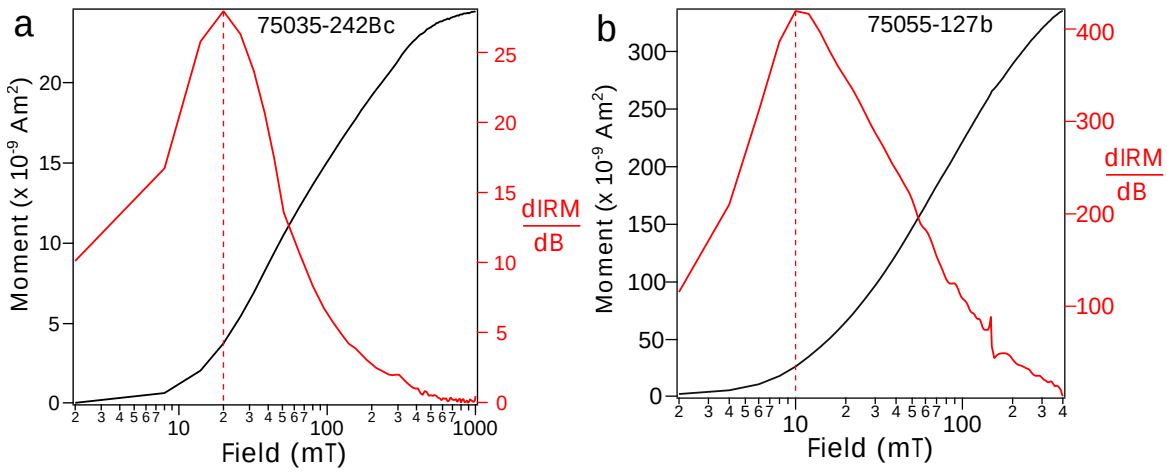


**Figure S10** | IRM acquisition curves. (a) Specimen 75035,242Bc contains magnetic carriers with a peak coercivity of $\sim$ 20 mT and a range of coercivities extending up to > 1000 mT. (b) Specimen 75055,127b contains magnetic carriers with a peak coercivity of $\sim$ 10 mT and a range of coercivities extending up to > 400 mT.

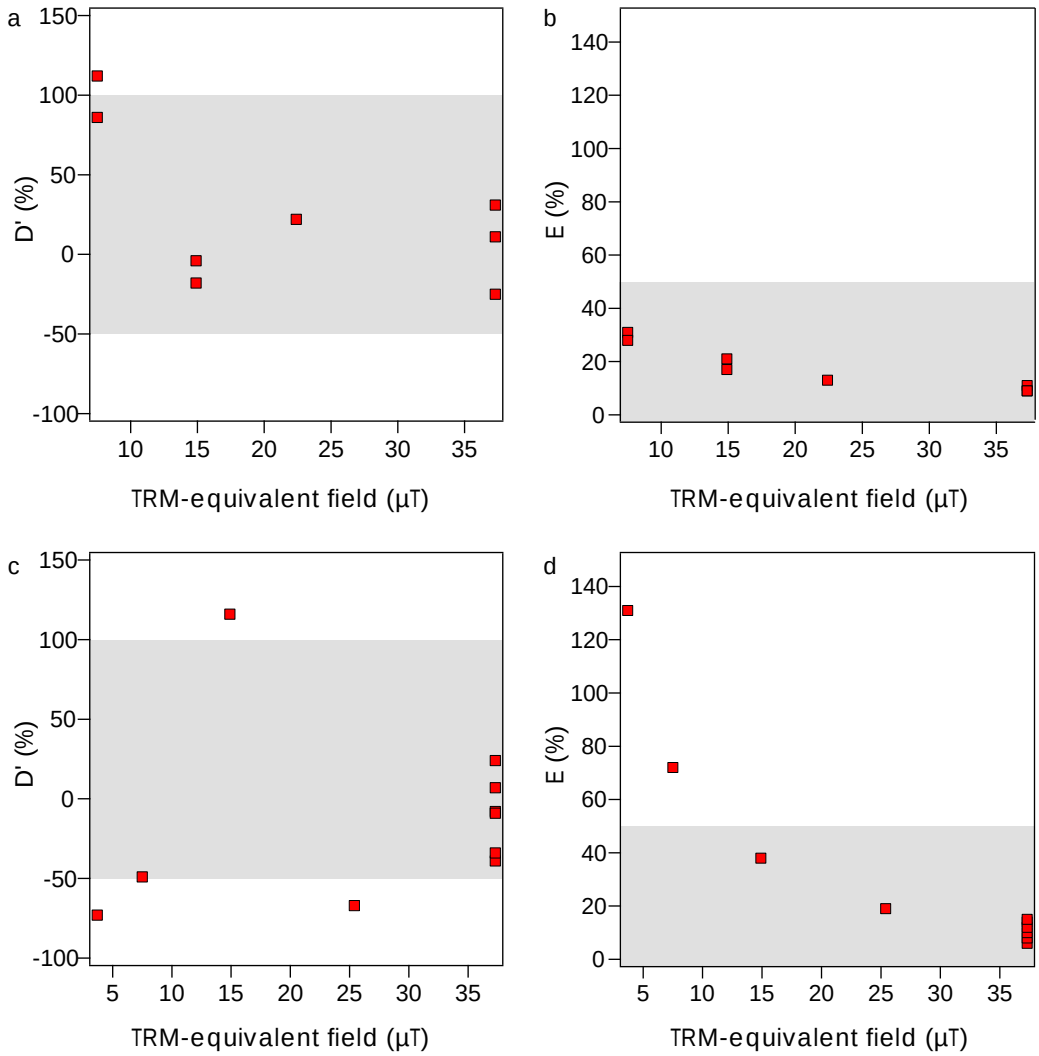


**Figure S11** | Paleointensity recording fidelity of 75035 and 75055. Results are tabulated in Table S4. (a) Difference metric, $D'$, for 75035. The grey region $-50\% > D' > 100\%$ indicates samples with adequate paleomagnetic fidelity. (b) Error metric, $E$, for 75035. The grey region $E < 50\%$ indicates samples with adequate paleomagnetic fidelity. (c)$D'$ for 75055. (d) $E$ for 75055.

## S2.3 Anisotropy of remanence and petrographic fabric analysis

Remanence anisotropy measurements were made for two reasons: to correct the recovered paleoinclinations for anisotropy effects within each specimen and to search for any evidence for a flow fabric in the sample defined by mutual orientation of the anisotropy axes between specimens. Note, however, that a flow fabric is not necessarily anticipated, given the predicted turbulent nature of low-viscosity lunar basaltic flows[38,39]. The remanence anisotropy of 7 specimens of 75035 and 6 specimens of 75055 were measured, all of which exhibited origin-trending HC components.

The degree of lineation $L$, foliation $F$ and anisotropy $P$ is reported for individual specimens (Tables S7 and S8). The recovered anisotropy ellipses were used to correct the NRM directions. We found that the degree of anisotropy is dependent on sample mass with smaller specimens tending to show a higher degree of anisotropy, consistent with previous mare basalt studies[5,40] (Figure S13). The degree of anisotropy in our individual specimens ($P = 1.0 - 1.5$) is similar to that measured for terrestrial basalts ($P = 1.1 - 1.8$)[41,42]. In both 75035 and 75055, there is no obvious fabric defined by the anisotropy axes of multiple specimens as indicated by the fact that Fisher dispersion factors $\kappa < 4$ for each axis (Figure S12).

| | Direction of applied ARM | | | | | | | | |
|---|---|---|---|---|---|---|---|---|---|
| **Specimen** | **1** | **2** | **3** | **4** | **5** | **6** | **7** | **8** | **9** |
| 75035,242Aa | $T_{lab}$ | $S_{lab}$ | $E_{lab}$ | $T_{lab}$-$S_{lab}$ | $B_{lab}$-$S_{lab}$ | $T_{lab}$-$E_{lab}$ | $B_{lab}$-$E_{lab}$ | $S_{lab}$-$E_{lab}$ | $N_{lab}$-$E_{lab}$ |
| 75035,242Ba | $N_{lab}$ | $W_{lab}$ | $T_{lab}$ | $N_{lab}$-$W_{lab}$ | $S_{lab}$-$W_{lab}$ | $T_{lab}$-$N_{lab}$ | $T_{lab}$-$S_{lab}$ | $T_{lab}$-$W_{lab}$ | $T_{lab}$-$E_{lab}$ |
| 75035,242Bb | $E_{lab}$ | $N_{lab}$ | $T_{lab}$ | $N_{lab}$-$E_{lab}$ | $N_{lab}$-$W_{lab}$ | $T_{lab}$-$E_{lab}$ | $T_{lab}$-$W_{lab}$ | $T_{lab}$-$N_{lab}$ | $T_{lab}$-$S_{lab}$ |
| 75035,242Bd | $N_{lab}$ | $W_{lab}$ | $T_{lab}$ | $N_{lab}$-$W_{lab}$ | $S_{lab}$-$W_{lab}$ | $T_{lab}$-$N_{lab}$ | $T_{lab}$-$S_{lab}$ | $T_{lab}$-$W_{lab}$ | $T_{lab}$-$E_{lab}$ |
| 75035,242Be | $E_{lab}$ | $S_{lab}$ | $B_{lab}$ | $S_{lab}$-$E_{lab}$ | $S_{lab}$-$W_{lab}$ | $B_{lab}$-$E_{lab}$ | $B_{lab}$-$W_{lab}$ | $T_{lab}$-$N_{lab}$ | $T_{lab}$-$S_{lab}$ |
| 75035,242Bf | $E_{lab}$ | $N_{lab}$ | $T_{lab}$ | $N_{lab}$-$E_{lab}$ | $N_{lab}$-$W_{lab}$ | $T_{lab}$-$E_{lab}$ | $T_{lab}$-$W_{lab}$ | $T_{lab}$-$N_{lab}$ | $T_{lab}$-$S_{lab}$ |
| 75035,242Bg | $N_{lab}$ | $W_{lab}$ | $T_{lab}$ | $N_{lab}$-$W_{lab}$ | $S_{lab}$-$W_{lab}$ | $T_{lab}$-$N_{lab}$ | $T_{lab}$-$S_{lab}$ | $T_{lab}$-$W_{lab}$ | $T_{lab}$-$E_{lab}$ |
| 75055,127Aa | $T_{lab}$ | $S_{lab}$ | $E_{lab}$ | $T_{lab}$-$S_{lab}$ | $B_{lab}$-$S_{lab}$ | $T_{lab}$-$E_{lab}$ | $B_{lab}$-$E_{lab}$ | $S_{lab}$-$E_{lab}$ | $N_{lab}$-$E_{lab}$ |
| 75055,127Ab | $T_{lab}$ | $S_{lab}$ | $E_{lab}$ | $T_{lab}$-$S_{lab}$ | $B_{lab}$-$S_{lab}$ | $T_{lab}$-$E_{lab}$ | $B_{lab}$-$E_{lab}$ | $S_{lab}$-$E_{lab}$ | $N_{lab}$-$E_{lab}$ |
| 75055,127Ac | $T_{lab}$ | $E_{lab}$ | $N_{lab}$ | $T_{lab}$-$E_{lab}$ | $B_{lab}$-$E_{lab}$ | $T_{lab}$-$N_{lab}$ | $B_{lab}$-$N_{lab}$ | $N_{lab}$-$E_{lab}$ | $N_{lab}$-$W_{lab}$ |
| 75055,127Ae | $N_{lab}$ | $W_{lab}$ | $T_{lab}$ | $N_{lab}$-$W_{lab}$ | $S_{lab}$-$W_{lab}$ | $T_{lab}$-$N_{lab}$ | $T_{lab}$-$S_{lab}$ | $T_{lab}$-$W_{lab}$ | $T_{lab}$-$E_{lab}$ |
| 75055,127a | $T_{lab}$ | $N_{lab}$ | $W_{lab}$ | $T_{lab}$-$N_{lab}$ | $B_{lab}$-$N_{lab}$ | $T_{lab}$-$W_{lab}$ | $B_{lab}$-$W_{lab}$ | $N_{lab}$-$W_{lab}$ | $S_{lab}$-$W_{lab}$ |
| 75055,127b | $T_{lab}$ | $N_{lab}$ | $W_{lab}$ | $T_{lab}$-$N_{lab}$ | $B_{lab}$-$N_{lab}$ | $T_{lab}$-$W_{lab}$ | $B_{lab}$-$W_{lab}$ | $N_{lab}$-$W_{lab}$ | $S_{lab}$-$W_{lab}$ |

**Table S5** | For AARM measurements, ARMs were applied in nine directions (shown by columns 1 – 9) corresponding to the anisotropy matrix. Specimens were mounted in different orientations with respect to laboratory coordinates and reconstructed to a mutual orientation in JSC coordinates after measuring. The demagnetization procedure between each ARM step is shown in Table S6.

| ARM direction | Demagnetization direction 1 | Demagnetization direction 2 | Demagnetization direction 3 |
|---|---|---|---|
| $E_{mag}$ | $N_{mag}$ | $T_{mag}$ | $E_{mag}$ |
| $N_{mag}$ | $E_{mag}$ | $T_{mag}$ | $N_{mag}$ |
| $T_{mag}$ | $N_{mag}$ | $E_{mag}$ | $T_{mag}$ |
| $NE_{mag}$ | $T_{mag}$ | $NW_{mag}$ | $NE_{mag}$ |
| $NW_{mag}$ | $NE_{mag}$ | $T_{mag}$ | $NW_{mag}$ |
| $TE_{mag}$ | $N_{mag}$ | $TW_{mag}$ | $TE_{mag}$ |
| $TW_{mag}$ | $TE_{mag}$ | $N_{mag}$ | $TW_{mag}$ |
| $TN_{mag}$ | $E_{mag}$ | $TS_{mag}$ | $TN_{mag}$ |
| $TS_{mag}$ | $TN_{mag}$ | $E_{mag}$ | $TS_{mag}$ |

**Table S6** | The orientation of the applied ARM and the three subsequent demagnetization steps used for AARM experiments. The first column shows the direction in which the ARM was applied. Samples were then demagnetized in the three orientations listed in the second, third and fourth columns, respectively.

| | 75035,242Aa | 75035,242Ba | 75035,242Bb | 75035,242Bd | 75035,242Be | 75035,242Bf | 75035,242Bg |
|---|---|---|---|---|---|---|---|
| $p_1$ | 658 | 998 | 1169 | 310 | 1404 | 1096 | 1117 |
| dec (°) | 107 | 075 | 080 | 099 | 065 | 232 | 278 |
| inc (°) | -23 | -37 | -46 | -23 | -05 | -42 | -03 |
| $p_2$ | 502 | 940 | 1140 | 252 | 1183 | 1066 | 838 |
| dec (°) | 040 | 075 | 329 | 033 | 147 | 319 | 024 |
| inc (°) | 42 | 53 | -20 | 43 | 60 | 04 | -78 |
| $p_3$ | 471 | 783 | 1038 | 229 | 1125 | 1054 | 731 |
| dec (°) | 358 | 345 | 043 | 349 | 338 | 045 | 008 |
| inc (°) | -40 | 00 | 38 | -39 | 31 | -47 | 12 |
| $L$ | 1.309 | 1.062 | 1.025 | 1.227 | 1.187 | 1.028 | 1.333 |
| $F$ | 1.067 | 1.200 | 1.098 | 1.102 | 1.051 | 1.011 | 1.146 |
| $P$ | 1.397 | 1.275 | 1.125 | 1.353 | 1.248 | 1.040 | 1.528 |
| Mass (mg) | 59.8 | 64.8 | 101.9 | 16.1 | 132.1 | 95.6 | 74.2 |

**Table S7** | AARM results for specimens of 75035. The first, second and third rows are the magnitude, declination and inclination (in JSC coordinates) of the maximum principal anisotropy axis $p_1$, respectively. The fourth, fifth and sixth rows are the magnitude, declination and inclination of the intermediate principal anisotropy axis, $p_2$, respectively. The seventh, eighth and ninth rows are the magnitude, declination and inclination of the minimum principal anisotropy axis, $p_3$, respectively. The directions of the principal axes for each specimen are plotted in Figure S12a. The tenth row is $L$, is the degree of lineation, the eleventh row is $F$, the degree of foliation and the twelfth row is $P$, the degree of anisotropy. The thirteenth row is the mass of the specimen.

| | 75055,127Aa | 75055,127Ab | 75055,127Ac | 75055,127Ae | 75055,127a | 75055,127b |
|---|---|---|---|---|---|---|
| $p_1$ | 1197 | 710 | 587 | 539 | 2705 | 4931 |
| dec (°) | 221 | 325 | 305 | 224 | 032 | 321 |
| inc (°) | -11 | -19 | -16 | -24 | 04 | 18 |
| $p_2$ | 1160 | 641 | 586 | 537 | 2374 | 4830 |
| dec (°) | 315 | 051 | 021 | 240 | 282 | 074 |
| inc (°) | -17 | 11 | 38 | 64 | 77 | 49 |
| $p_3$ | 1017 | 512 | 499 | 514 | 2364 | 4656 |
| dec (°) | 281 | 291 | 233 | 316 | 123 | 038 |
| inc (°) | 68 | 66 | 47 | -06 | 12 | -34 |
| $L$ | 1.031 | 1.107 | 1.001 | 1.004 | 1.139 | 1.020 |
| $F$ | 1.140 | 1.251 | 1.173 | 1.043 | 1.004 | 1.037 |
| $P$ | 1.176 | 1.386 | 1.175 | 1.048 | 1.144 | 1.059 |
| Mass (mg) | 102.5 | 62.6 | 58.3 | 54.9 | 271.0 | 641.0 |

**Table S8** | Anisotropy of ARM results for specimens of 75055. The first, second and third rows are the magnitude, declination and inclination (in JSC coordinates) of the maximum principal anisotropy axis $p_1$, respectively. The fourth, fifth and sixth rows are the magnitude, declination and inclination of the intermediate principal anisotropy axis, $p_2$, respectively. The seventh, eighth and ninth rows are the magnitude, declination and inclination of the minimum principal anisotropy axis, $p_3$, respectively. The directions of the principal axes for each specimen are plotted in Figure S12b. The tenth row is $L$, is the degree of lineation, the eleventh row is $F$, the degree of foliation and the twelfth row is $P$, the degree of anisotropy. The thirteenth row is the mass of the specimen.

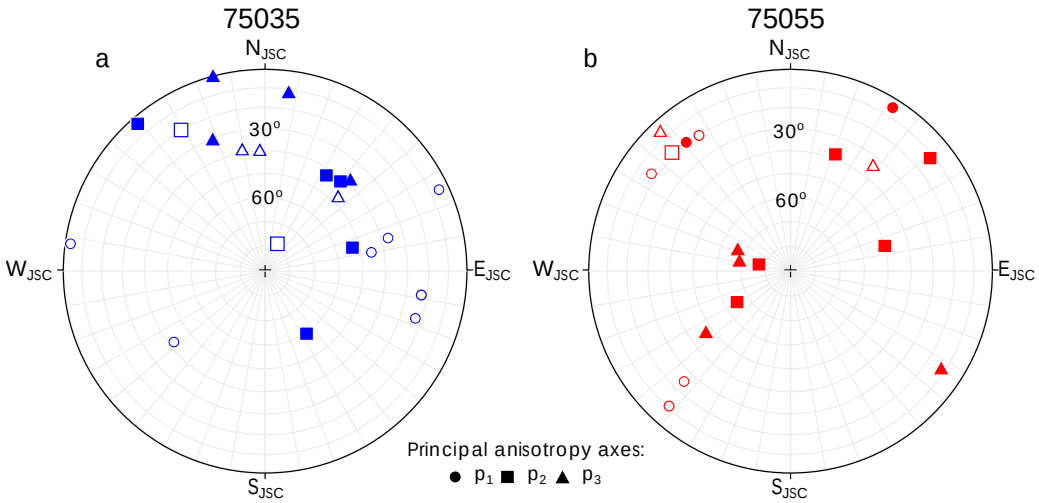


**Figure S12** | Equal area polar stereonet projections showing the minimum $p_3$ (triangles), intermediate $p_2$ (squares) and maximum $p_1$ (circles) principal anisotropy axes for specimens of (a) 75035 and (b) 75055 in JSC coordinates. Solid symbols are in the lower hemisphere, open symbols are in the upper hemisphere. There is no clear fabric defined by the anisotropy axes, Fisher precision parameters are < 4 for all axes.

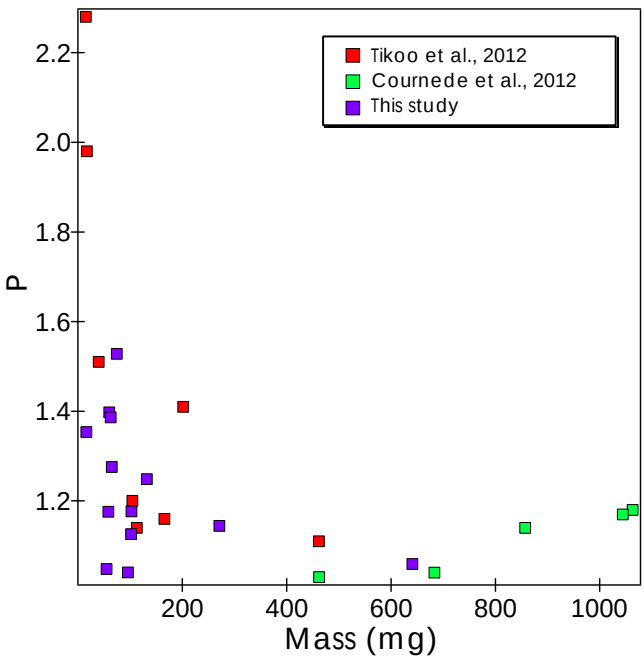


**Figure S13** | The degree of anisotropy, $P$, recovered for AARM measurements as a function of sample mass. Our results are consistent with previous studies of lunar basalts conducted by ref. 5 and ref. 40.

Hand samples and thin sections were also examined for evidence of any flow fabrics. Rose diagrams of plagioclase crystal orientations were found to have a circular variance of 0.73 and 0.98 for 75035

and 75055, respectively, where the circular variance is 0 for perfect alignment in one direction and 1 for an entirely uniform distribution (Figure S14). The lack of fabric defined within the mineralogy of the samples is consistent with the fact that well-aligned fabrics only develop in laminar flows, whereas the flow of lunar basalts is expected to be turbulent[38,39].

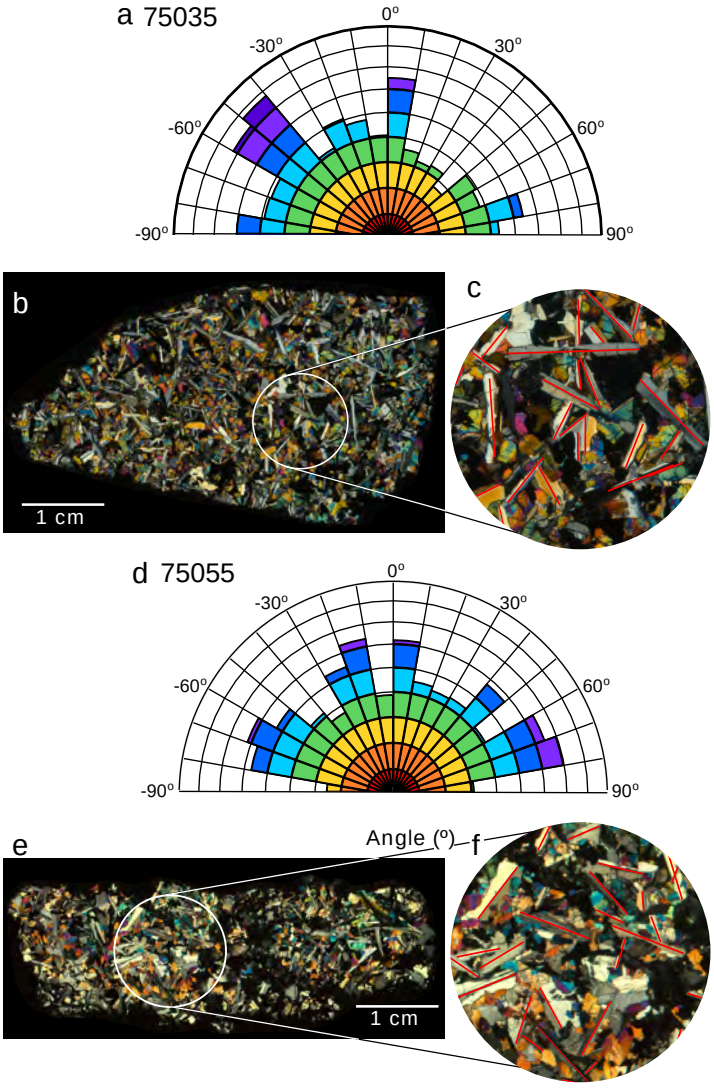


**Figure S14** | Analysis of the orientation of plagioclase crystals assessed from photomicrographs of thin sections 75035,84 and 75055,46. (a) Equal area rose diagram of plagioclase orientation distributions for 75035. The circular variance of the distribution is 0.73 ($N$ = 86). (b) Cross-polarized transmitted light image of thin section 75035. (c) Magnified region of thin section 75035. Red lines show the identified plagioclase orientations used for orientation analysis. (d) Equal area rose diagram of plagioclase orientation distributions for 75055. The circular variance of the distribution is 0.98 ($N$ = 127). (e) and (f) are the same as (b) and (c) for 75055.

## S2.4 The magnetic inclination of 75035 and 75055

The inclination of 75035 in present-day lunar coordinates (18 ± 14°) was calculated from four origin-trending, high coercivity components with MAD < 30°. An additional four specimens (75035,242Af, 75035,242Bd, 75035,242Be and 75035,242Bg) did not pass our criteria, but define a similar high coercivity direction. When these samples are also taken into account, we recover an inclination in present-day lunar coordinates of 15 ± 13°.

The paleoinclination of 75055 (34 ± 10°) was calculated from five origin-trending, high coercivity components with MAD < 30°. It should be noted that even the specimens that do not meet these criteria define a similar direction. If they are added to the anisotropy-corrected mean, we recover an inclination in lunar paleohorizontal coordinates of 33 ± 8°. Similarly, if we remove specimen 75055,127c2 which is on the threshold of our origin-trending criteria, we recover an inclination of 34 ± 13°. Therefore our inclination results are robust regardless of the exact selection criteria we use to include or exclude specimens.

| Specimen | JSC | | Lunar geographic | | Lunar paleohorizontal | |
|---|---|---|---|---|---|---|
| | Dec(°) | Inc(°) | Dec(°) | Inc(°) | Dec(°) | Inc(°) |
| Pre-anisotropy correction | | | | | | |
| 75055,127b | 220 | 05 | 339 | -01 | 341 | -37 |
| 75055,127c1 | 221 | 14 | 336 | 07 | 336 | -29 |
| 75055,127c2 | 216 | 04 | 336 | -04 | 337 | -40 |
| 75055,127Aa | 225 | 26 | 333 | 19 | 333 | -17 |
| 75055,127Ac | 205 | 013 | 323 | -01 | 320 | -36 |
| Post-anisotropy correction | | | | | | |
| 75055,127b | 220 | 02 | 341 | -04 | 343 | -40 |
| 75055,127c1 | 221 | 14 | 336 | 07 | 336 | -29 |
| 75055,127c2 | 216 | 04 | 336 | -04 | 337 | -40 |
| 75055,127Aa | 226 | 21 | 336 | 16 | 337 | -20 |
| 75055,127Ac | 211 | 01 | 333 | -09 | 333 | -45 |

**Table S9** | The recovered declination and inclination for specimens of 75055 with origin-trending components pre- and post-anisotropy correction. The first column is the specimen. The second and third columns are the declination and inclination in JSC coordinates, repspectively. The fourth and fifth column are in lunar geographic coordinates and the sixth and seventh columns are in lunar paleohorizontal coordinates.

## S2.5 Lunar paleointensities

Our AF demagnetization of specimens of 75035 and 75055 revealed a non-origin-trending LC component of NRM that was removed by 0 – 11 mT (Figure 2 and Table S11). The LC components are highly scattered within each parent sample (Figure 3). LC components are likely a viscous remanent magnetization (VRM) acquired on Earth during sampling and storage, which has also been observed for other lunar samples[25]. The scattered nature can be explained by varying VRM acquisition rates for magnetic carriers of different grain sizes. Once the LC overprints were removed, we found that six non-bandsawn specimens of 75035 and five specimens of 75055 each contained a final origin-trending HC component that was blocked up to 40 – 60 mT and essentially unidirectional within each parent sample (Figure 2 and Table S11). The Fisher mean anisotropy-corrected HC direction for these six specimens of 75035 is 030°/11° in present-day lunar coordinates (see Methods Table 1 for definitions and descriptions of coordinate systems) with a 95% confidence interval $\alpha_{95} = 16°$. The Fisher mean anisotropy-corrected HC direction for five specimens of 75055 in present-day lunar coordinates is 334°/02° with $\alpha_{95} = 11°$. In lunar paleohorizontal coordinates, the HC component of 75055 has a paleoinclination of $I_{LPH} = 34°$, $\alpha_{95} = 11°$, and an estimated Fisher precision parameter $\kappa = 46.0$, where the uncertainty is estimated from the scatter in the HC directions among individual specimens.

We measured mean HC paleointensities of 50.7 ± 13.5 $\mu$T and 57.0 ± 17.3 $\mu$T ($1\sigma$ standard error of 4 and 8 subsamples) for 75035 and 75055, respectively, using the ARM method (Figure S16 and Table S10). The calculated confidence intervals for individual specimens reported in Table S9 are based on 95% confidence intervals from the least-squares fits of NRM lost versus ARM lost during AF demagnetization. The relatively large scatter in recovered paleointensities is attributed to the small specimen sizes: most are $<$ 200 mg and several mm in diameter, not much larger than their mean silicate grain size[13]. In particular, this likely explains their heterogeneous magnetic recording fidelities (Table S4). Note that the confidence intervals listed for each paleointensity do not take into account systematic uncertainties due to the poorly known ratio of ARM to TRM. The latter $2\sigma$ uncertainties are estimated to be a factor of $\sim 5$[43], such that the true range of paleointensities is 10 – 250 $\mu$T and 11 – 285 $\mu$T for 75035 and 75055, respectively. Therefore, the paleointensity estimates for 75035 and 75055 are both within error of the mean value of 77 $\mu$T measured from six samples of age 3.5 – 4.2 Ga[5,44,45,46]. They thereby provide additional evidence that $>$ 3.5 Ga ago, the Moon had an active dynamo generating a strong magnetic field. Even the lower limit on our recovered paleointensity ($\sim$ 10 $\mu$T) exceeds the field strength predicted by convective dynamo scaling laws and is barely compatible with a dynamo intermittently reaching this strength over an integrated time of just 30 Ma[47]. Furthermore, this minimum paleointensity is still a factor of 2 stronger than the weak paleointensities measured between $\sim$ 3.5 – 1 Ga ago, and at least an order of magnitude stronger than the weakest fields that can be reasonably attributed to an active dynamo[23,24,25].

| Specimen | Experiment | Paleointensity ($\mu$T) |
|---|---|---|
| 75035,242Aa | 100 $\mu$T ARM | 33.1 $\pm$ 5.5 |
| 75035,242Ae | 100 $\mu$T ARM | 101.3 $\pm$ 7.9 |
| 75035,242Af | 100 $\mu$T ARM | 23.7 $\pm$ 2.4 |
| 75035,242Bc | 100 $\mu$T ARM | 47.7 $\pm$ 4.7 |
| | **Mean $\pm$ 1$\sigma$** | **50.7 $\pm$ 13.5** |
| 75055,127a | 50 $\mu$T ARM | 18.2 $\pm$ 5.7 |
| 75055,127b | 100 $\mu$T ARM | 50.0 $\pm$ 10.6 |
| 75055,127c1 | 200 $\mu$T ARM | 50.4 $\pm$ 5.2 |
| 75055,127c2 | 200 $\mu$T ARM | 84.3 $\pm$ 11.9 |
| 75055,127Aa | 100 $\mu$T ARM | 33.3 $\pm$ 2.6 |
| 75055,127Ab | 100 $\mu$T ARM | 12.2 $\pm$ 8.3 |
| 75055,127Ac | 100 $\mu$T ARM | 34.4 $\pm$ 4.2 |
| 75055,127Ae | 100 $\mu$T ARM | 173.1 $\pm$ 14.3 |
| | **Mean $\pm$ 1$\sigma$** | **57.0 $\pm$ 17.3** |

**Table S10** | Paleointensity estimates for HC components for samples 75035 and 75055. The first column is the measured specimen. The second column shows the strength of the applied ARM used for the paleointensity estimate. The third column shows the estimated paleointensity and 2$\sigma$ uncertainty calculated from a two-tailed Student's $t$ test but does not take into account the factor of 5 uncertainty associated with the calibration factor $f'$[43]. Paleointensities were calculated over the HC field range shown in Table S11.

| Specimen | Mass (mg) | Magnetization ($\times 10^{-6}$ Am$^2$kg$^{-1}$) | HC component: Unanchored to origin Dec (°) | Inc (°) | MAD (°) | DANG(°) | AF (mT) | O-trending? | Anchored to origin Dec (°) | Inc (°) | MAD (°) | DANG(°) | LC component Dec (°) | Inc (°) | MAD (°) | DANG (°) | AF (mT) |
|---|---|---|---|---|---|---|---|---|---|---|---|---|---|---|---|---|---|
| 75035,242Aa | 59.8 | 2.78 | 155 | 60 | 26 | 33 | 5 – 30 | × | | | | | 354 | -66 | 23 | 155 | 0 – 5 |
| 75035,242Ab | 203.1 | 0.64 | | | | | | | | | | | | | | | |
| 75035,242Ac | 232.8 | 2.17 | 312 | 42 | 27 | 49 | 6.5 – 31 | × | | | | | 358 | 77 | 28 | 72 | 0 – 6.5 |
| *75035,242Ad** | 322.3 | 7.45 | 302 | 74 | 10 | 10 | 7 – 25 | ✓ | 295 | 84 | 4 | 0 | 247 | 42 | 6 | 37 | 0 – 7 |
| 75035,242Ae | 46.6 | 17.3 | 93 | 45 | 18 | 15 | 11.5 – 47 | ✓ | 76 | 38 | 7 | 0 | 69 | 31 | 11 | 14 | 0 – 11 |
| 75035,242Af | 188 | 1.99 | 48 | 33 | 27 | 33 | 10 – 23.5 | × | | | | | 191 | 16 | 29 | 96 | 0 – 10 |
| 75035,242Ag | 169.3 | 1.46 | | | | | | | | | | | 205 | 58 | 17 | 24 | 0 – 3.5 |
| *75035,242Ah** | 277.8 | 9.83 | 199 | 71 | 8 | 6 | 6 – 25 | ✓ | 193 | 77 | 3 | 0 | 222 | 32 | 6 | 38 | 0 – 7 |
| 75035,242Ba | 64.9 | 8.03 | 85 | 58 | 28 | 6 | 11 – 33 | ✓ | 84 | 63 | 8 | 0 | 86 | -49 | 11 | 93 | 0 – 5 |
| 75035,242Bb | 102 | 4.48 | | | | | | | | | | | 102 | 70 | 15 | 14 | 0 – 14 |
| 75035,242Bc | 65.3 | 6.34 | 107 | 54 | 26 | 11 | 10.5 – 40 | ✓ | 112 | 43 | 11 | 0 | 345 | -32 | 37 | 137 | 0 – 7 |
| 75035,242Bd | 16.1 | 12.05 | 94 | 59 | 47 | 44 | 10 – 40 | ✓ | 55 | 24 | 20 | 0 | 115 | 42 | 15 | 33 | 0 – 3.5 |
| 75035,242Be | 132.1 | 4.44 | 52 | 16 | 43 | 8 | 10 – 40 | ✓ | 51 | 24 | 16 | 0 | 58 | 41 | 14 | 9 | 0 – 6 |
| 75035,242Bf | 95.6 | 6.54 | 92 | 32 | 11 | 3 | 4 – 40 | ✓ | 93 | 30 | 5 | 0 | 178 | -53 | 20 | 110 | 0 – 3.5 |
| 75035,242Bg | 74.2 | 6.31 | 94 | 40 | 15 | 27 | 16 – 45 | × | | | | | 39 | 62 | 19 | 33 | 0 – 11 |
| 75055,127a | 271 | 4.03 | 210 | 25 | 20 | 27 | 2.5 – 24 | × | | | | | 353 | 48 | 10 | 103 | 0 – 2 |
| 75055,127b | 641 | 3.95 | 220 | 5 | 18 | 11 | 9.5 – 84 | ✓ | 215 | 6 | 13 | 0 | 37 | 49 | 5 | 126 | 0 – 1.5 |
| 75055,127c1 | 156 | 4.03 | 221 | 14 | 18 | 11 | 4 – 35 | ✓ | 217 | 3 | 8 | 0 | 294 | 39 | 30 | 70 | 0 – 1.5 |
| 75055,127c2 | 166 | 7.29 | 216 | 4 | 14 | 14 | 10 – 28 | ✓ | 211 | 17 | 4 | 0 | 341 | -20 | 34 | 131 | 0 – 9.5 |
| 75055,127Aa | 102.5 | 14.63 | 225 | 26 | 20 | 13 | 2.5 – 45 | ✓ | 237 | 33 | 9 | 0 | 183 | 2 | 4 | 44 | 0 – 2 |
| 75055,127Ab | 62.6 | 4.15 | | | | | | | | | | | | | | | |
| 75055,127Ac | 54.9 | 6.19 | 205 | 13 | 26 | 15 | 4.5 – 39 | ✓ | 220 | 9 | 13 | 0 | 89 | -48 | 20 | 124 | 0 – 4 |
| 75055,127Ad | 8.3 | 3.25 | | | | | | | | | | | | | | | |
| 75055,127Ae | 58.3 | 20.58 | 219 | 8 | 7 | 14 | 7.5 – 55 | × | | | | | 92 | -66 | 27 | 101 | 0 – 6.5 |

*samples with bandsaw overprint

**Table S11** | LC and HC components identified during AF demagnetization of specimens of 75035 and 75055. Declinations and inclinations are in laboratory coordinates. In the case where no reasonable fit could be made, the row is left blank. The first column lists the specimen. The second column lists the mass of the specimen and the third lists the specific magnetization of the NRM. The fourth, fifth, sixth and seventh columns list the declination, inclination, MAD and deviation angle, respectively, for unanchored high coercivity components; the eighth column lists the AF range over which the component was fitted. The ninth column lists whether the identified high coercivity component was origin-trending (MAD>DANG), and for those that were, the tenth, eleventh, twelfth and thirteenth column are the declination, inlincation, MAD and deviation angle, respectively, for high coercivity components anchored to the origin. The fourteenth, fifteenth, sixteenth and seventeenth columns list the declination, inclination, MAD, deviation angle and AF range, respectively, for any identified low coercivity components. Origin-trending specimens with an unanchored MAD $< 30°$ were used to calculate HC directions and are highlighted in red.

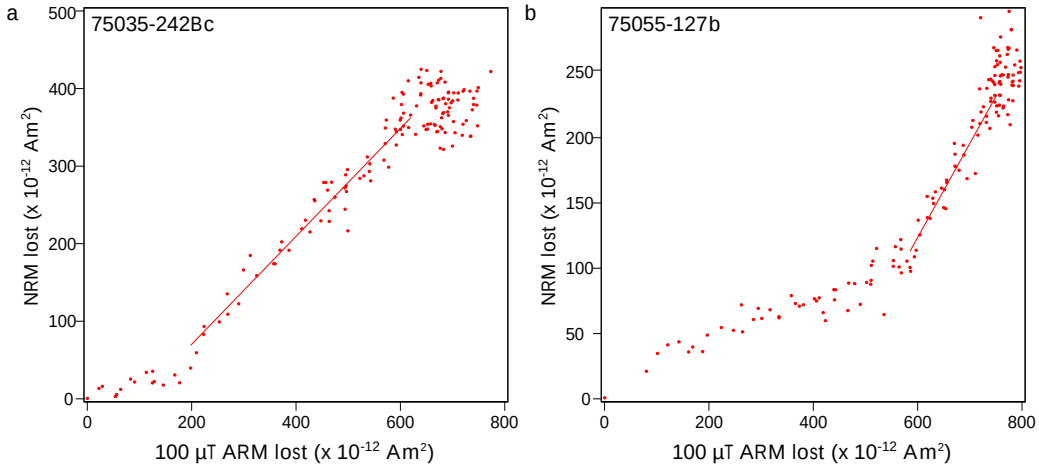


**Figure S15** | Examples of ARM paleointensity estimates for 75035 and 75055. NRM lost versus 100 $\mu$T ARM lost is plotted for progressive AF demagnetization. (a) ARM paleointensity plot for specimen 75035,242Bc. (b) ARM paleointensity plot for specimen 75055,127b.

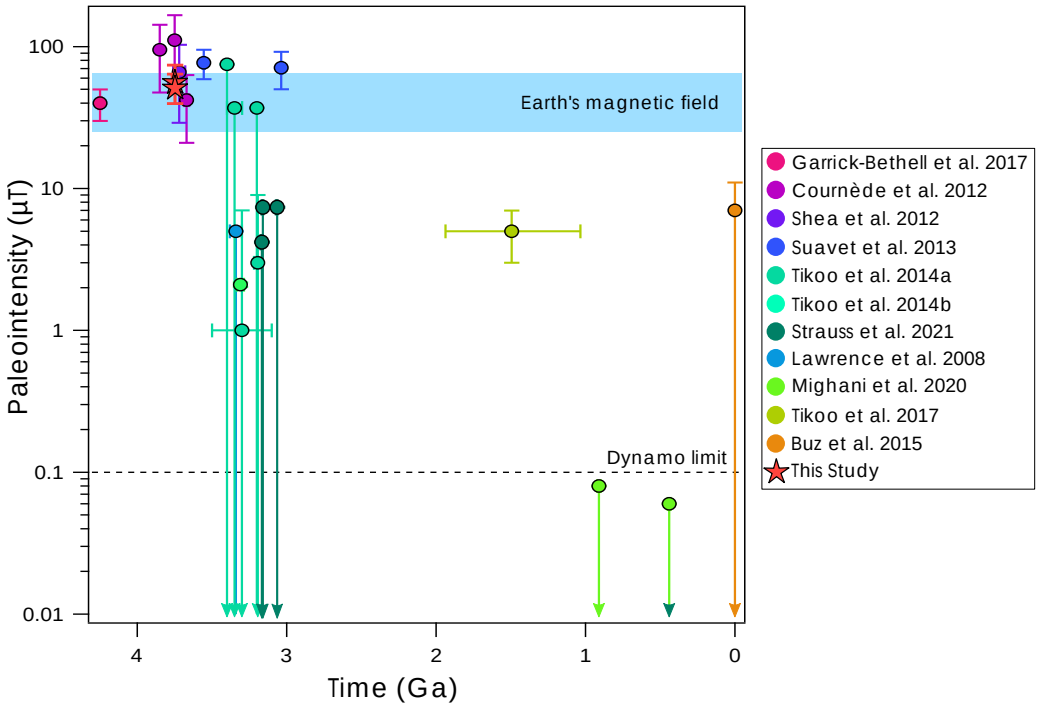


**Figure S16** | Summary of the paleointensity measurements on Apollo samples colour coded by study from refs. 5, 23, 24, 25, 28, 45, 46, 48, 49, 50, 51. All age and paleointensity uncertainties shown are from the original studies, except the age uncertainties for ref. 25 which were recalculated by ref. 23. The blue region is the strength of Earth's present day magnetic field. The dashed black line is the weakest field that could be driven by a lunar dynamo (see ref. 23). Paleointensities calculated for 75035 and 75055 are shown by red stars.

# S3 Paleopole Reconstructions and True Polar Wander

## S3.1 Paleopole reconstructions using crustal magnetic anomalies

Orientable lunar samples for paleomagnetic study are extremely rare, and therefore alternative approaches have been used to determine the geometry of the ancient lunar magnetic field. Numerous previous studies have attempted to constrain the geometry of the ancient magnetic field using spacecraft measurements of the crustal magnetic field. Although some such studies found support for the presence of a selenocentric axial dipole geometry from the clustering of some paleopoles, the paleopoles as a whole are spread over the entire surface of the Moon[8,52]. The large scatter of the paleopoles is likely in part a consequence of the fact that, even for a uniformly magnetized source with a single component of magnetization, inverted paleopoles depend on assumptions about the source, depth and susceptibility of magnetization, resulting in nonunique magnetization solutions[53,54]. Furthermore, if the crust has multiple components of magnetization acquired at different times throughout lunar history, then even if a paleopole could be uniquely recovered from the net magnetization, it would not correspond to the paleopoles associated with any of the composite magnetization events. Finally, it is difficult to determine the age of paleopoles inferred from orbital data given the uncertainty of using crater counting ages to date deep crustal magnetization sources and the lack of direct radiometric constraints. We therefore argue that paleodirections constrained directly via the paleomagnetic study of orientable samples can significantly reduce the ambiguity in ancient lunar magnetic field geometries constrained from crustal magnetic anomalies.

## S3.2 Independent evidence for true polar wander

The topography and gravity of the Moon suggest that the rotation axis may have reoriented by $36 \pm 4°$ from an ancient paleopole location of $54 \pm 5$ °N, $309 \pm 6$ °E since the Cassini state transition[44]. True polar wander has also been suggested to explain variability in the directions of crustal magnetization[52,55]. Lunar hydrogen deposits, which may represent ancient polar ice deposits, are also observed in two distinct, antipodal locations offset from the current spin poles, suggesting that the Moon may have experienced a significant degree of true polar wander[6]. We consider the paleopoles recovered using a variety of approaches 3.5 – 4 Ga and find consistency with our results (Figure S17). Our results constrain two small circles corresponding to the location of the north magnetic pole at 3.7 Ga (Figure S18).

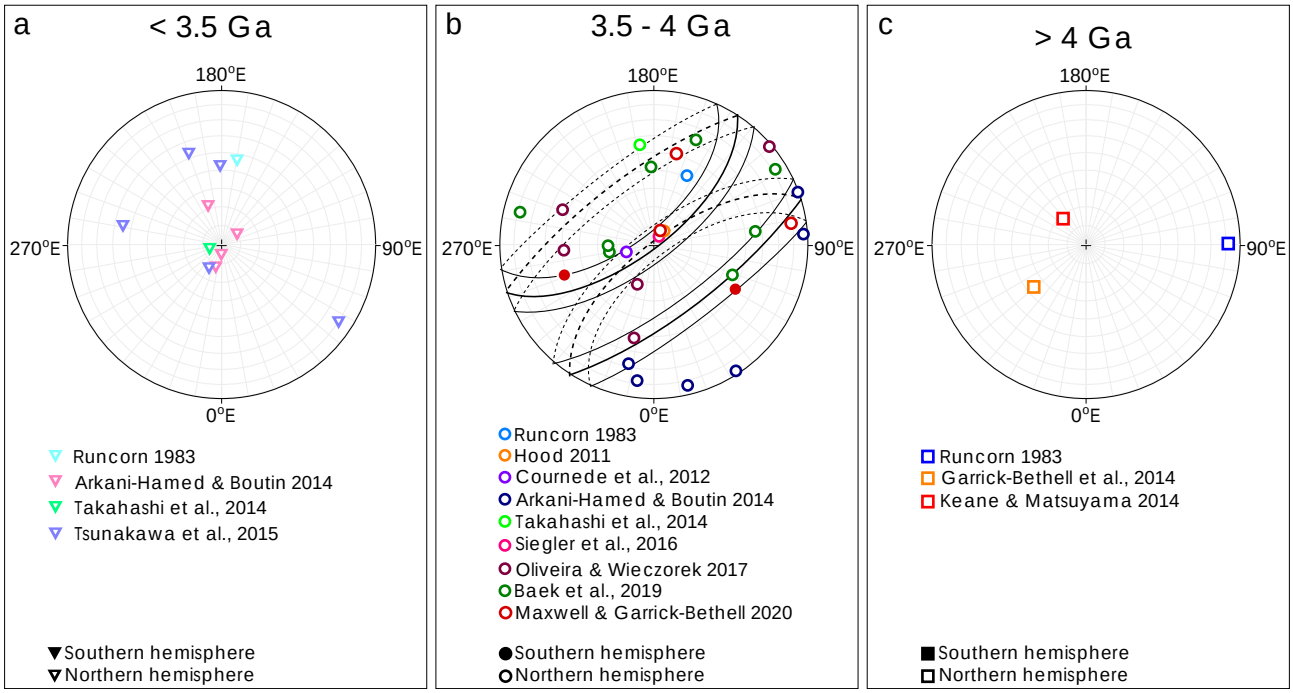


**Figure S17** | A summary of north paleopole locations summarized from the literature. (a) Paleopole locations for < 3.5 Ga are generally found to be aligned along the present day spin axis[9,10,56,57]. (b) Paleopole locations 3.5 – 4 Ga[5,6,7,8,9,10,52,56,58] which have ages broadly similar to our samples (the permitted North pole locations from our paleoinclination are shown by the two small circles with 95% confidence bounds). (c) Paleopole locations > 4 Ga[10,44,59].

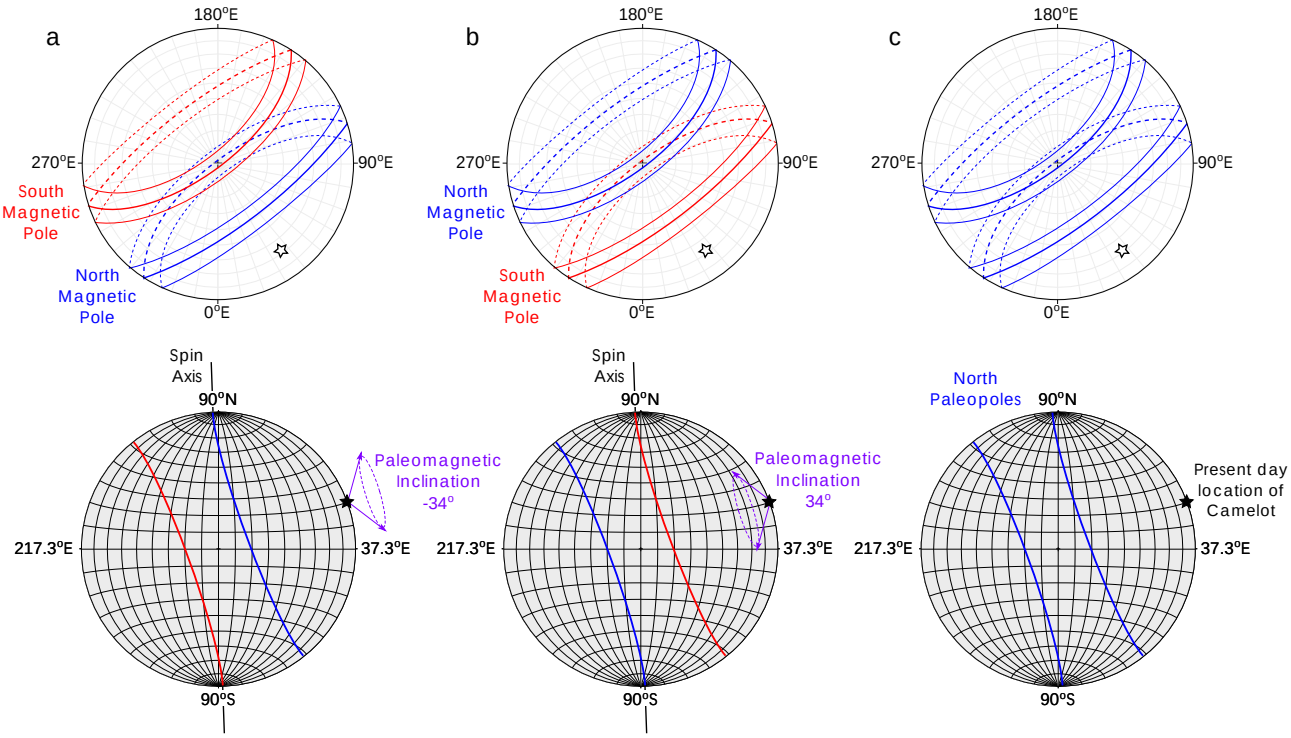


**Figure S18** | Schematic diagrams show the plausible true polar wander paths permitted by our measured paleoinclination for 75055. The blue and red small circles show the permitted locations of the north and south magnetic poles, respectively. We assume a selenocentric axial dipole such that the paleopole location represents the position of the ancient spin axis. (a) If the measured magnetic inclination at Camelot crater is negative, Camelot was in the northern hemisphere 3.7 Ga ago and was located closest the north magnetic pole. (b) If the measured magnetic inclination at Camelot crater is positive, Camelot was in the southern hemisphere 3.7 Ga ago and was located closest to the south magnetic pole. (c) Considering Camelot crater at its present day location, the small circles are shown for the allowed north pole locations for Camelot crater in either the northern or southern hemisphere 3.7 Ga ago.

## S4 Reconciling the high lunar $Ro_l$ with a dipolar magnetic field

The relative contributions of an axial dipole and multipolar terms to a dynamo field are thought to be influenced by the local Rossby number, $Ro_l$, which quantifies the ratio of inertial to Coriolis forces for characteristic flow scales within the core[60,61]. Most bodies with active dynamos in the solar system today are estimated to have $Ro_l$ below a critical value of $\sim 0.12$. Furthermore all bodies other than the ice giants have dipole-dominated instantaneous fields with dipole tilts $< 10°$, consistent with Coriolis forces strongly influencing their geometries[61,62]. For the Earth's time-averaged field, this is manifested by behavior described by Equation (1).

Synchronous rotation of the Moon was likely established early in lunar history, such that by 3.7 Ga ago the rotation rate was sufficiently slow ($\sim 5 \times 10^{-6}$ rad s$^{-1}$) that its $Ro_l$ would have reached a value of $\sim 2$, suggesting that the field in the core was dominantly nondipolar[61]. In particular, simulations of dynamos with $Ro_l$ exceeding a critical value of $\sim 0.1$ have found that such dynamos have a dipolarity, $f_{dip} = \frac{B_d}{B_{nd}} = 0.001 - 0.1$, where $B_d$ and $B_{nd}$ are the intensities of the dipole (e.g., spherical harmonic degree $l = 1$) and non-dipole (e.g., $l > 1$) components of the field, respectively. On the other hand, the small size of the lunar core ($\sim \frac{1}{7}$ of the body's radius[63]) should lead to significant attenuation of the higher order multipolar terms at the lunar surface. Conservatively assuming that at the top of the lunar core the multipolar field was dominated by the quadrupolar term, such that $B_d = 0.001 - 0.1$ and the quadrupolar part of the field was $B_q = 0.9 - 0.999$, then given that dipole (e.g., degree $l = 1$) and quadrupole terms ($l = 2$) fall off as $r^{-(l+2)}$ for distance from the top of the core, $r$, the predicted field at the surface would still be significantly multipolar ($f_{dip} \sim 0.007 - 0.44$). Therefore, we do not expect that the lunar dynamo must have followed Equation (1).

Even so, a high $Ro_l$ does not by itself preclude a dipolar surface magnetic field geometry. The multipolar state implied by the high $Ro_l$ only applies to the field-generating region in the core, whereas paleomagnetic observations only constrain the surface field. For example, as has been proposed for Mercury which has a dominantly dipolar field in spite of its high estimated $Ro_l$[64,65,66], a subadiabatic, stably stratified layer may have existed at the top of the lunar core (e.g. ref. 63) that suppressed multipolar field components due to their higher time variability relative to that of the low-degree field. In addition, if the core is stratified, then the thermal and compositional buoyancy forces must be considered separately to account for double-diffusive convection. However, previous estimates of the lunar $Ro_l$ were calculated using a co-density approach, which may only be applicable to turbulent, well-mixed cores[61]. It has been demonstrated that using a double-diffusion approach instead can drastically change the predicted surface magnetic fields[67]. Additionally, previous estimates of the lunar $Ro_l$ assumed that dynamo action is convection-driven[61] but this assumption may not apply for a different mechanism of dynamo generation, such as precession[68,69].

# S5 Distinguishing between sources of the lunar magnetic field in light of new paleoinclination results

Given the difficulties associated with generating the observed strong lunar magnetic field with a thermal or thermochemical core dynamo, a diversity of other dynamo as well as non-dynamo mechanisms have been proposed to have magnetized the lunar surface. We consider these mechanisms here for completeness, but acknowledge that they are less likely given our current understanding of the lunar interior. If the lunar surface was magnetized by Earth's time-averaged geocentric axial dipole[3] a uniform inclination equal to the lunar latitude would be observed (Figure 1e). Another possibility is that the lunar surface was magnetized by the interplanetary magnetic field (IMF), which is expected, on average, to have been instantaneously aligned along the plane of the lunar equator (Figure 1f)[70]. Magnetic fields amplified by basin-forming impacts in the solar wind, although recently shown to be unable to explain lunar paleointensities[71], were predicted to have inclinations close to horizontal (0°) over much of the lunar surface and close to vertical (90°) at the basin antipodes (Figure 1g)[72]. Magnetic fields generated locally by smaller impacts would likely have scattered inclinations that cluster around 0° for near-vertical impacts in near-zero ambient fields (Figures 1h)[73,74,75,76]. Near-horizontal inclinations might be expected for a thermoelectric dynamo generated by adjacent lava basins[4], while near-vertical inclinations might be expected for a unipolar dynamo in an isolated lava basin[3] (Figure 1i,j). Cometary impacts perhaps generated predominantly horizontal inclinations across the lunar surface (Figure 1k)[3,77,78].

External field sources from either Earth's ancient dynamo or the IMF are expected to produce inclinations that are too low or high at the latitude of Camelot crater, respectively, under the assumption that their orientations were similar to those observed today (Figure 4a). Other sources of magnetization such as impacts and thermoelectric dynamos (Figure 1g-k) are also apparently inconsistent with our paleoinclination results.

## S5.1 Multipolar magnetic fields

The high value of $Ro_l$ for the lunar core resulting from its slow rotation rate suggests the dynamo should be multipolar, at least in the dynamo-generating region (main text Figure 1b)[61]. Alternatively, it has been suggested that rather than originating in the core, the lunar magnetic field may have been generated by a basal magma ocean dynamo (main text Figure 1c,d), which would be closer to the lunar surface which would favour a higher degree of multipolarity at the surface relative to that of a deeper-seated core dynamo. As such, the measured paleoinclination may not constrain the axial dipole field component. The inclination of the magnetic field at Camelot crater depends on the zonal dipolar, quadrupolar and octupolar contributions to the magnetic field[79] as:

$$\tan I = \frac{2\cos\theta + G2(4.5\cos^2\theta - 1.5) + G3(10\cos^3\theta - 6\cos\theta)}{\sin\theta + G2(3\cos\theta\sin\theta) + G3(7.5\cos^2\theta\sin\theta - 1.5\sin\theta)} \tag{3}$$

where $I$ is the inclination and $\theta$ is the colatitude which we take to be 69.8° (the current colatitude of Camelot crater, assuming no true polar wander since remanence acquisition), $G2$ is the zonal quadrupole to zonal dipole field ratio, and $G3$ is the zonal octupole to zonal dipole field ratio. Both low ($G2 < 0.2$ and $G3 < 0.2$) and high ($0 < G2 < 1$ and $0.3 < G3 < 0.75$) contributions from the quadrupo-

lar and octupolar components give results consistent with our measured inclinations. Therefore, even when considering just the first two nondipolar zonal terms to the multipole field expansion, the lunar dynamo is permitted to be highly multipolar based on our measured paleoinclination, consistent with either a dynamo originating in the core or a basal magma ocean.

### S5.2 External magnetic field sources

We consider whether the lunar surface could plausibly have been magnetized by Earth's magnetic field. We assume the Earth had an active magnetic field $\sim 3.7$ Ga ago, although there is currently no robust record beyond 3.5 Ga ago[80,81,82,83]. Under the assumption that the mean field represented an axial dipole, and given that the Earth and Moon were likely already tidally locked by this time[84], such a field would have uniformly magnetized the lunar surface, with $I = \lambda$ (main text Figure 1e). In this case, the inclination of the magnetic field at Camelot crater would be much lower than the observed paleoinclinations, confirming the Earth's magnetic field is an unlikely source of lunar magnetization. In addition, given the distance between the Earth and the Moon, the Earth would impart negligible paleointensities ($\sim 1\ \mu$T assuming the Earth's magnetic field is similar to today, and the Moon was at the Roche limit) on the lunar surface.

We also consider the influence of the IMF and its ability to magnetize the lunar surface. The IMF constantly changes direction, but the time-averaged field is predominantly aligned in the lunar equatorial plane[70], where $I = 90 - \lambda$ (main text Figure 1f). Assuming a similar geometry at 3.7 Ga, the IMF would therefore have generated a much higher inclination than that observed at Camelot crater, ruling out this source of magnetization. In addition, because the Moon rotates 360° with respect to the IMF every orbit around the Earth, the mean field at Camelot should average out to a null field.

### S5.3 Impact-generated magnetic fields

It has been suggested that the lunar surface may have been magnetized by impact events[85]. In particular, it was proposed that basin-forming impacts could generate a plasma field which expands around the Moon, focusing the magnetic field at the antipodal point to the impact[72]. Although recent magnetohydrodynamic simulations indicate that such a mechanism likely cannot explain the high paleointensities recorded by lunar samples[71], we still compare its predictions with our measurements as an experimental test of this hypothesis. Independent of latitude, crustal magnetization generated by impact events would lead to near-vertical paleoinclinations (here we assume they are perfectly vertical) (main text Figure 1g,h). Our recovered paleoinclination at Camelot crater is $\sim 50°$ shallower, suggesting this is an unlikely source of magnetization.

We also consider whether the magnetizations of 75035 and 75055 are compatible with having been acquired during the Camelot crater formation event at 500 Ma ago. Because the dynamo had likely ceased by this time[23], the only plausible field source would be the local crustal field. We assume that the local crustal field was the same as that today and was not modified by the cratering event. We test this hypothesis in two ways: first, we compare the measured paleoinclination to that of the crustal field and second, we estimate whether the samples could have been sufficiently heated or shocked by the impact to acquire a stable NRM. The crustal magnetic field at an altitude of 30 km above the lunar surface has been measured by the Lunar Prospector fluxgate magnetometer[86]. Using both sequential and correlative field models we found that the inclination of the crustal magnetic field at Camelot crater

is $\sim 47°$ which differs by more than $2\sigma$ from our measured paleoinclination from 75055. However, a limitation of this analysis is that this requires downward continuation which will not accurately predict fine-scale surface fields.

We now consider whether the samples would likely have been remagnetized by the impact. We conducted impact simulations using the iSALE-2D shock physics code[87,88,89] to evaluate the potential for shock metamorphism and heating from the formation of Camelot crater. The impact simulations were run to match the dimensions of Camelot crater, with a final rim-to-rim diameter of $\sim$ 600 m and original depth of $\sim$ 120 m[90]. To achieve these dimensions, a 20 m diameter, spherical impactor travelling at 15 km $s^{-1}$ (a typical lunar impact velocity[91,92]) perpendicular to the target was used. Both the impactor and target were assumed to have zero porosity and were simulated using an ANEOS equation of state for basalt[93]. Simulations were run with a spatial resolution of 2 m.

Our simulations suggest low peak pressures ($<$ 1 GPa) and post-shock temperatures ($<$ 280 K) associated with the Camelot crater-forming impact event at the inferred formation locations of 75035 and 75055. Results are shown for crater formation at the transient cavity stage (Figure S19). Only a small volume of material, proximal to the point of impact experiences significant shock pressures or post-shock temperature increases. However, attenuation would be much greater in a porous target (e.g., one or more thick layers of intra-basalt regolith layers) so an even smaller volume may experience temperatures $>$ 100 °C greater than normal[94]. Temperatures are therefore unlikely to exceed the Curie temperature given the relatively low porosity of mare basalts[95]. The peak shock pressure is also too low to influence the NRM of the samples. Paleomagnetic signals preserved in samples prior to cratering at this locality are therefore likely to be unperturbed.

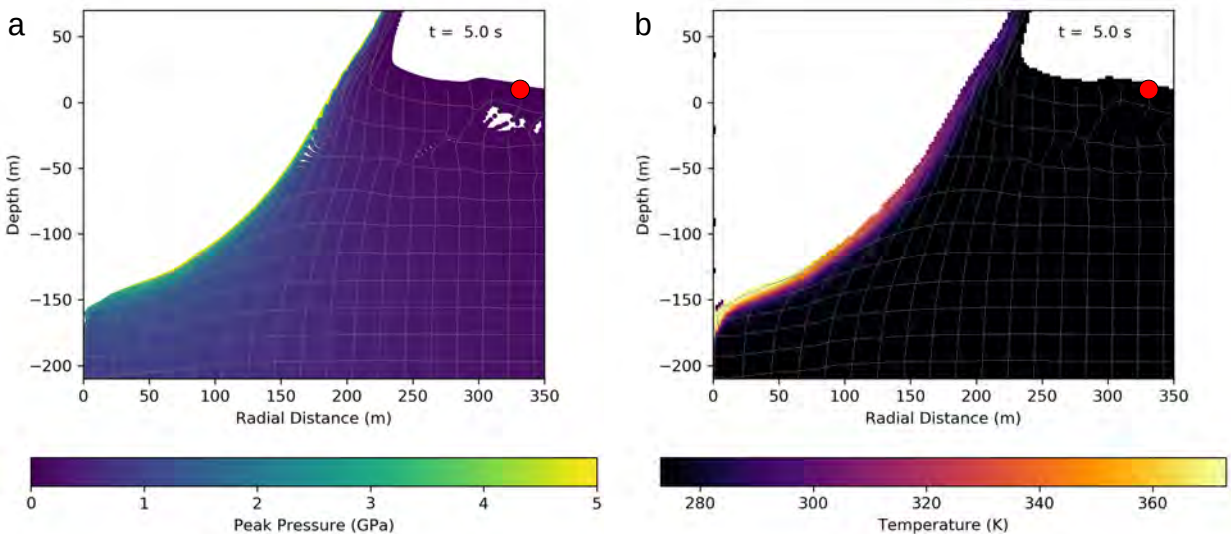


**Figure S19** | Impact simulations for a 20 m diameter, spherical impactor with a velocity of 15 km $s^{-1}$. Simulations show the peak pressure and temperature 5 seconds after the impact event. Both the target and impactor are basaltic in composition. The red dot indicates the approximate position of 75035 and 75055 at Station 5. (a) The bulk of the target material is only very weakly shocked, with peak pressures predominantly < 2 GPa. (b) Only the edge of the impact basin experiences significant heating, while the bulk of the target material does not exceed temperatures of 280 K.

# References


[1] Scheinberg, A. L., Soderlund, K. M. & Elkins-Tanton, L. T. A basal magma ocean dynamo to explain the early lunar magnetic field. *Earth and Planetary Science Letters* **492**, 144–151 (2018).

[2] Hood, L. L. & Artemieva, N. A. Antipodal effects of lunar basin-forming impacts: Initial 3D simulations and comparisons with observations. *Icarus* **193**, 485–502 (2008).

[3] Daily, W. & Dyal, P. Theories for the origin of lunar magnetism. *Physics of the Earth and Planetary Interiors* **20**, 255–270 (1979).

[4] Dyal, P., Parkin, C. W. & Daily, W. D. Global lunar crust: Electrical conductivity and thermoelectric origin of remanent magnetism. *8th Lunar Science Conference* 767–783 (1977).

[5] Cournède, C., Gattacceca, J. & Rochette, P. Magnetic study of large Apollo samples: Possible evidence for an ancient centered dipolar field on the Moon. *Earth and Planetary Science Letters* **331-332**, 31–42 (2012).

[6] Siegler, M. A. *et al.* Lunar true polar wander inferred from polar hydrogen. *Nature* **531**, 480–484 (2016).

[7] Maxwell, R. E. & Garrick-Bethell, I. Evidence for an ancient near-equatorial lunar dipole from higher precision inversions of crustal magnetization. *Journal of Geophysical Research* **125**, 1–20 (2020).

[8] Hood, L. L. Central magnetic anomalies of Nectarian-aged lunar impact basins: Probable evidence for an early core dynamo. *Icarus* **211**, 1109–1128 (2011).

[9] Takahashi, F., Tsunakawa, H., Shimizu, H., Shibuya, H. & Matsushima, M. Reorientation of the early lunar pole. *Nature Geoscience* **7**, 409–412 (2014).

[10] Runcorn, S. K. Lunar magnetism, polar displacements and primeval satellites in the Earth-Moon system. *Nature* **304**, 589–596 (1983).

[11] Meyer, C. Lunar Sample Compendium (2010).

[12] Brown, G. M., Peckett, A., Emeleus, C. H., Phillips, R. & Pinsent, R. H. Petrology and mineralogy of Apollo 17 mare basalts. *Proceedings of the Lunar Science Conference* **6**, 1–13 (1975).

[13] Donohue, P. H. & Neal, C. R. Quantitative textural analysis of ilmenite in Apollo 17 high-titanium mare basalts. *Geochimica et Cosmochimica Acta* **149**, 115–130 (2015).

[14] Paces, J. B. *et al.* A strontium and neodymium isotopic study of Apollo 17 high-Ti mare basalts: Resolution of ages, evolution of magmas, and origins of source heterogeneities. *Geochimica et Cosmochimica Acta* **55**, 2025–2043 (1991).

[15] Turner, G. & Cadogan, P. H. Possible effects of 39Ar recoil in 40Ar-39Ar dating. *Proceedings of the Lunar Science Conference* **5**, 1601–1615 (1974).

[16] Turner, G., Cadogan, P. H. & Yonge, C. J. Argon selenochronology. *Proceedings of the Lunar Science Conference* **4**, 1889–1914 (1973).

[17] Snape, J. F. *et al.* The timing of basaltic volcanism at the Apollo landing sites. *Geochimica et Cosmochimica Acta* **266**, 29–53 (2019). URL `https://doi.org/10.1016/j.gca.2019.07.042`.

[18] Usselman, T. M., Lofgren, G. E., Williams, R. J. & Donaldson, C. H. Experimentally reproduced textures and mineral chemistries of high-titanium mare basalts. *Proceedings of the Lunar Science Conference* **6**, 997–1020 (1975).

[19] Kirsten, T., Horn, P. & Heymann, D. Chronology of the Taurus-Littrow region I: Ages of two major rock types from the Apollo 17-site. *Earth and Planetary Science Letters* **20**, 125–130 (1973).

[20] Schaal, R. B., Horz, F. & Thompson, T. D. Shock metamorphism of granulated lunar basalt. *Proceedings of the Lunar and Planetary Science Conference* (1979).

[21] Ahrens, T. J., O'Keefe, J. D. & Gibbons, R. V. Shock compression of a recrystallized anorthositic rock from Apollo 15. *Proceedings of the Fourth Lunar Science Conference* **3**, 2575–2590 (1973).

[22] Schaal, R. B. & Hörz, F. Shock metamorphism of lunar and terrestrial basalts. *Proceedings of the Lunar Science Conference* **8**, 1697–1729 (1977).

[23] Mighani, S. *et al.* The end of the lunar dynamo. *Science Advances* **6**, 1–8 (2020).

[24] Tikoo, S. M. *et al.* Decline of the lunar core dynamo. *Earth and Planetary Science Letters* **404**, 89–97 (2014).

[25] Tikoo, S. M. *et al.* A two-billion-year history for the lunar dynamo. *Science Advances* **3**, e1700207 (2017).

[26] Pearce, G. Magnetism of the Apollo 17 samples. *Lunar and Planetary Science Conference* **5**, 590 (1974).

[27] Sugiura, N., Strangway, D. & Pearce, G. Heating experiments and paleointensity determinations. *Proceedings of the Lunar and Planetary Science Conference* **9**, 3151–3163 (1978).

[28] Lawrence, K., Johnson, C., Tauxe, L. & Gee, J. Lunar paleointensity measurements: Implications for lunar magnetic evolution. *Physics of the Earth and Planetary Interiors* **168**, 71–87 (2008).

[29] Potter, D. K. Novel magnetic techniques for rapidly detecting palaeomagnetically important single-domain iron particles and obtaining directional palaeomagnetic data from "unoriented" lunar rock samples. *Canadian Aeronautical Space Journal* **57**, 12–23 (2011).

[30] Wolfe, E. W. *et al.* Investigation of the Taurus-Littrow Valley : Apollo 17 Landing Site The Geologic. *Geological Survey Professional Paper 1080* (1981).

[31] Archanjo, C. J. & Launeau, P. Magma flow inferred from preferred orientations of plagioclase of the Rio Cearfi-Mirim dyke swarm (NE Brazil) and its AMS significance. *Geological Society Special Publication* **238**, 285–298 (2004).

[32] Geoffroy, L., Callot, J. P., Aubourg, C. & Moreira, M. Magnetic and plagioclase linear fabric discrepancy in dykes : a new way to define the flow vector using magnetic foliation. *Terra Nova* **14**, 183–190 (2002).

[33] Schindelin, J. *et al.* Fiji: an open-source platform for biological-image analysis. *Nature Methods* **9**, 676–82 (2012).

[34] Schindelin, J., Rueden, C. T., Hiner, M. C. & Eliceiri, K. W. The ImageJ ecosystem: An open platform for biomedical image analysis. *Molecular Reproduction and Development* **82**, 518–529 (2015).

[35] Muxworthy, A. R. & Williams, W. Critical single-domain grain sizes in elongated iron particles: Implications for meteoritic and lunar magnetism. *Geophysical Journal International* **202**, 578–583 (2015).

[36] Chowdhary, S. K., Collinson, D. W., Stephenson, A. & Runcorn, S. Further investigations into lunar paleointensity determinations. *Physics of the Earth and Planetary Interiors* 121–122 (1987).

[37] Bryson, J. F., Weiss, B. P., Harrison, R. J., Herrero-Albillos, J. & Kronast, F. Paleomagnetic evidence for dynamo activity driven by inward crystallisation of a metallic asteroid. *Earth and Planetary Science Letters* **472**, 152–163 (2017).

[38] Schobel, S. & de Wall, H. AMS–NRM interferences in the Deccan basalts: Toward an improved understanding of magnetic fabrics in flood basalts. *Journal of Geophysical Research* **119**, 2651–2678 (2014).

[39] Whitford-Stark, J. L. Factors influencing the morphology of volcanic landforms: An earth-moon comparison. *Earth Science Reviews* **18**, 109–168 (1982).

[40] Tikoo, S. M. *et al.* Magnetic fidelity of lunar samples and implications for an ancient core dynamo. *Earth and Planetary Science Letters* **337-338**, 93–103 (2012).

[41] Biedermann, A. R., Jackson, M., Stillinger, M. D., Bilardello, D. & Feinberg, J. M. Anisotropy of full and partial anhysteretic remanence across different rock types: 1—Are partial anhysteretic remanence anisotropy tensors additive? *Tectonics* **39**, 1–16 (2020).

[42] Biedermann, A. R., Jackson, M., Bilardello, D. & Feinberg, J. M. Anisotropy of full and partial anhysteretic remanence across different rock types: 2—Coercivity dependence of remanence anisotropy. *Tectonics* **39**, 1–19 (2020).

[43] Weiss, B. P. & Tikoo, S. M. The lunar dynamo. *Science* **346** (2014).

[44] Garrick-Bethell, I., Perera, V., Nimmo, F. & Zuber, M. T. The tidal-rotational shape of the Moon and evidence for polar wander. *Nature* **512**, 181–184 (2014).

[45] Shea, E. K. *et al.* A long-lived lunar core dynamo. *Science* **335**, 453–456 (2012).

[46] Suavet, C. *et al.* Persistence and origin of the lunar core dynamo. *Proceedings of the National Academy of Sciences* **110**, 8453–8 (2013).

[47] Evans, A. J., Tikoo, S. M. & Andrews-Hanna, J. C. The case against an early lunar dynamo powered by core convection. *Geophysical Research Letters* 98–107 (2018).

[48] Garrick-Bethell, I., Weiss, B. P., Shuster, D. L., Tikoo, S. M. & Tremblay, M. M. Further evidence for early lunar magnetism from troctolite 76535. *Journal of Geophysical Research* **122**, 76–93 (2017).

[49] Tikoo, S. M., Weiss, B. P., Shuster, D. L. & Fuller, M. D. How long did the lunar core dynamo persist? *Lunar and Planetary Science Conference* **45**, 1–2 (2014).

[50] Strauss, B. E., Tikoo, S. M., Gross, J., Setera, J. B. & Turrin, B. Constraining the decline of the lunar dynamo field at 3.1 Ga through paleomagnetic analyses of Apollo 12 mare basalts. *Journal of Geophysical Research* 1–21 (2021).

[51] Buz, J., Weiss, B. P., Tikoo, S. M., Shuster, D. L. & Gattacceca, J. Magnetism of a very young lunar glass. *Journal of Geophysical Research: Planets* (2015).

[52] Oliveira, J. S. & Wieczorek, M. A. Testing the axial dipole hypothesis for the Moon by modeling the direction of crustal magnetization. *Journal of Geophysical Research* **122**, 383–399 (2017).

[53] Vervelidou, F. & Lesur, V. Unveiling Earth's hidden magnetization. *Geophysical Research Letters* **45**, 12,283–12,292 (2018).

[54] Gerhards, C. On the reconstruction of inducing dipole directions and susceptibilities from knowledge of the magnetic field on a sphere. *Inverse Problems in Science and Engineering* **27**, 37–60 (2019).

[55] Nayak, M., Hemingway, D. & Garrick-Bethell, I. Magnetization in the South Pole-Aitken basin: Implications for the lunar dynamo and true polar wander. *Icarus* **286**, 153–192 (2017).

[56] Arkani-Hamed, J. & Boutin, D. Analysis of isolated magnetic anomalies and magnetic signatures of impact craters: Evidence for a core dynamo in the early history of the Moon. *Icarus* **237**, 262–277 (2014).

[57] Tsunakawa, H., Takahashi, F., Shimizu, H., Shibuya, H. & Matsushima, M. Surface vector mapping of magnetic anomalies over the Moon using Kaguya and Lunar Prospector observations. *Journal of Geophysical Research* **120**, 1160–1185 (2015).

[58] Baek, S. M., Kim, K. H., Garrick-Bethell, I. & Jin, H. Magnetic anomalies within the Crisium Basin: magnetization directions, source depths, and ages. *Journal of Geophysical Research* **124**, 223–242 (2019).

[59] Keane, J. T. & Matsuyama, I. Evidence for lunar true polar wander and a past low-eccentricity, synchronous lunar orbit. *Geophysical Research Letters* **41**, 6610–6619 (2014).

[60] Gastine, T., Duarte, L. & Wicht, J. Dipolar versus multipolar dynamos: The influence of the background density stratification. *Astronomy and Astrophysics* **546**, 1–13 (2012).

[61] Olson, P. & Christensen, U. R. Dipole moment scaling for convection-driven planetary dynamos. *Earth and Planetary Science Letters* **250**, 561–571 (2006).

[62] Stevenson, D. J. Planetary magnetic fields: Achievements and prospects. *Space Science Reviews* **152**, 651–664 (2009).

[63] Weber, R. C., Lin, P.-Y., Garnero, E., Williams, Q. C. & Lognonné, P. Seismic detection of the lunar core. *Science* **331**, 309–12 (2011).

[64] Cao, H. *et al.* A dynamo explanation for Mercury's anomalous magnetic field. *Geophysical Research Letters* **41**, 4127–4134 (2014).

[65] Christensen, U. R. A deep dynamo generating Mercury's magnetic field. *Nature* **444**, 1056–1058 (2006).

[66] Takahashi, F., Shimizu, H. & Tsunakawa, H. Mercury's anomalous magnetic field caused by a symmetry-breaking self-regulating dynamo. *Nature Communications* **10**, 1–8 (2019).

[67] Manglik, A., Wicht, J. & Christensen, U. R. A dynamo model with double diffusive convection for Mercury's core. *Earth and Planetary Science Letters* **289**, 619–628 (2010).

[68] Dwyer, C. A., Stevenson, D. J. & Nimmo, F. A long-lived lunar dynamo driven by continuous mechanical stirring. *Nature* **479**, 212–214 (2011).

[69] Stys, C. & Dumberry, M. A past lunar dynamo thermally driven by the precession of its inner core. *Journal of Geophysical Research* 1–20 (2020).

[70] Oran, R., Weiss, B. P. & Cohen, O. Were chondrites magnetized by the early solar wind? *Earth and Planetary Science Letters* **492**, 222–231 (2018).

[71] Oran, R., Weiss, B. P., Shprits, Y., Miljković, K. & Tóth, G. Was the moon magnetized by impact plasmas? *Science Advances* **6**, 1–11 (2020).

[72] Hood, L. L. Magnetic field and remanent magnetization effects of basin-forming impacts on the Moon. *Geophysical Research Letters* **14**, 844–847 (1987).

[73] Hide, R. Comments on the moon's magnetism. *The Moon* **4** (1972).

[74] Srnka, L. J. *et al.* Magnetic field and shock effects and remanent magnetization in a hypervelocity impact experiment. *Earth and Planetary Science Letters* **42**, 127–137 (1979).

[75] Crawford, D. A. & Schultz, P. H. The production and evolution of impact-generated magnetic fields. *International Journal of Impact Engineering* **14**, 205–216 (1993).

[76] Crawford, D. A. Simulations of magnetic fields produced by asteroid impact: Possible implications for planetary paleomagnetism. *International Journal of Impact Engineering* **137**, 1–8 (2020).

[77] Gold, T. & Soter, S. Cometary impact and the magnetization of the Moon. *Planetary and Space Science* **24**, 45–54 (1976).

[78] Schultz, P. H. & Srnka, L. J. Cometary collisions on the Moon and Mercury. *Nature* **284**, 22–26 (1980).

[79] Merrill, R. T., McElhinny, M. & McFadden, P. L. *The Magnetic Field of the Earth: Paleomagnetism, the Core and the Deep Mantle* (Academic Press, 1996).

[80] Biggin, A. J. *et al.* Palaeomagnetism of Archaean rocks of the Onverwacht Group, Barberton Greenstone Belt (southern Africa): Evidence for a stable and potentially reversing geomagnetic field at ca. 3.5Ga. *Earth and Planetary Science Letters* **302**, 314–328 (2011).

[81] Usui, Y., Tarduno, J. A., Watkeys, M., Hofmann, A. & Cottrell, R. D. Evidence for a 3.45-billion-year-old magnetic remanence: Hints of an ancient geodynamo from conglomerates of South Africa. *Geochemistry, Geophysics, Geosystems* **10**, 1–16 (2009).

[82] Weiss, B. P. *et al.* Secondary magnetic inclusions in detrital zircons from the Jack Hills , Western Australia and implications for the origin of the geodynamo microscopy. *Geology* **46** (2018).

[83] Tang, F. *et al.* Secondary magnetite in ancient zircon precludes analysis of a Hadean geodynamo. *Proceedings of the National Academy of Sciences* **116**, 407–412 (2019).

[84] Ward, W. Past orientation of the lunar spin axis. *Science* **189**, 377–380 (1975).

[85] Lin, R. P., Anderson, K. A. & Hood, L. L. Lunar surface magnetic field concentrations antipodal to young large impact basins. *Icarus* **74**, 529–541 (1988).

[86] Purucker, M. E. & Nicholas, J. B. Global spherical harmonic models of the internal magnetic field of the Moon based on sequential and coestimation approaches. *Journal of Geophysical Research* **115**, 1–14 (2010).

[87] Amsden, A. A., Ruppel, H. M. & Hirt, C. W. SALE : A Simplified ALE Computer Program for Fluid Flow at All Speeds. *Los Alamos National Laboratories Report* 101 (1980).

[88] Collins, G. S., Melosh, H. J. & Ivanov, B. A. Modeling damage and deformation in impact simulations. *Meteoritics and Planetary Science* **231**, 217–231 (2004).

[89] Wünnemann, K., Collins, G. S. & Melosh, H. J. A strain-based porosity model for use in hydrocode simulations of impacts and implications for transient crater growth in porous targets. *Icarus* **180**, 514–527 (2006).

[90] Schmitt, H. H. *et al.* Revisiting the field geology of Taurus–Littrow. *Icarus* **298**, 2–33 (2017).

[91] Johnson, B. C. *et al.* The formation of lunar multi-ring basins. *Science* **354**, 441–444 (2016).

[92] Le Feuvre, M. & Wieczorek, M. A. Nonuniform cratering of the Moon and a revised crater chronology of the inner Solar System. *Icarus* **214**, 1–20 (2011).

[93] Pierazzo, E., Artemieva, N. A. & Ivanov, B. Starting Conditions for Hydrothermal Systems Underneath Martian Craters: Hydrocode Modeling. *Geological Society of America Special Paper* **384**, 443–457 (2005).

[94] Wünnemann, K., Collins, G. S. & Osinski, G. R. Numerical modelling of impact melt production in porous rocks. *Earth and Planetary Science Letters* **269**, 530–539 (2008).

[95] Kiefer, W. S., MacKe, R. J., Britt, D. T., Irving, A. J. & Consolmagno, G. J. The density and porosity of lunar rocks. *Geophysical Research Letters* **39**, 1–5 (2012).